Electronic Thesis and Dissertation Repository

9-19-2018 3:45 PM

Non-Pilot Protection of the Inverter-Dominated AC Microgrid

Houman Lahiji, *The University of Western Ontario*

Supervisor: Badrkhani Ajaei, Firouz, *The University of Western Ontario*
A thesis submitted in partial fulfillment of the requirements for the Master of Engineering
Science degree in Electrical and Computer Engineering
© Houman Lahiji 2018

Abstract

The main objective of this research is to develop reliable non-pilot protection and control strategies for the inverter-dominated microgrid. First, an improved Proportional-Derivative (PD) droop control strategy is proposed for enhanced disturbance response of the inverter-dominated AC microgrid. The proposed strategy significantly improves microgrid dynamic response and stability without requiring communication between distributed energy resources. Moreover, the impacts of large startup currents of induction motors on the stability and power quality of the inverter-dominated microgrid are investigated and recommendations for minimizing the associated adverse effects are made.

Subsequently, a fast, selective, and reliable protection strategy for the inverter-dominated microgrid is introduced. The proposed protection strategy utilizes phase- and sequence-domain protective elements for reliable detection of symmetrical and asymmetrical faults without the need for communication signals or adaptive relays settings. The protection strategy is robust against the grid-connection mode of the microgrid and enables fuse protection of laterals. It can also be implemented on the existing commercially available relays. The acceptable performance of the proposed protection and control strategies is verified through numerous fault studies conducted on a realistic study system in the PSCAD/EMTDC software environment. Additionally, the proposed protection strategy is implemented in a SEL-351 relay and evaluated using the SEL-AMS industrial relay testing platform.

Keywords: Inverter-dominated Microgrid Protection, Negative-Sequence Directional Element, Motor Starting in the Islanded Microgrid, Voltage and Frequency Regulation.

To my parents.

Acknowledgement

I would like to first and foremost express my sincerest gratitude to my diligent supervisor, Dr. Firouz Badrkhani Ajaei. His unwavering guidance and support at every stage of my thesis motived me to make momentous progress on my research and generally in the field of electrical engineering. I also want to thank the examining committee, Dr. Rajiv Varma, Dr. Pirathayini Srikantha, and Dr. Mohammad Reza Najafi for their time and considerations. Finally, I want to thank my parents for their support of my higher education.

Table of Contents

List of Figures

List of Tables

List of Appendices

List of Abbreviations

BESS	Battery Energy Storage System
CTI	Coordination Time Interval
DER	Distributed Energy Resource
ECA	Element Characteristics Angle
IIDER	Inverter-Interfaced Distributed Energy Resource
IPR	Interface Protection Relay
LL	Line-to-Line
LLG	Line-to-Line-to-Ground
GSC	Grid-Side Converter
MPPT	Maximum Power Point Tracking
MPR	Microgrid Protection Relay
MSC	Machine-Side Converter
MTA	Maximum Torque Angle
NSDE	Negative-Sequence Directional Element
OC	Over-Current
PCC	Point of Common Coupling
PD	Proportional-Derivative
PMSG	Permanent Magnet Synchronous Generator
PSDE	Positive-Sequence Directional Element
PV	PhotoVoltaic
RES	Renewable Energy System
SFS	Sandia Frequency Shift
SLG	Single Line-to-Ground
TCT	Total Clearing Time
VSC	Voltage-Sourced Converter
WT	Wind Turbines
ZSDE	Zero-Sequence Directional Element

Chapter 1

1   Introduction

1.1   Background

A microgrid is a small power system containing Distributed Energy Resources (DERs) and loads within a clearly defined electrical boundary that can operate in the grid-connected and islanded modes [1]-[3]. The islanding is accomplished by opening a switch at the Point of Common Coupling (PCC), allowing the microgrid to operate independently even during faults and disturbances in the utility grid [1]. The microgrid technology offers significant advantages such as improving the power quality, reliability and efficiency, as well as facilitating grid integration of DERs [4], [5].

The most common DERs in a microgrid are Renewable Energy Systems (RESs), e.g., PhotoVoltaic (PV) generation systems and Wind Turbines (WT), and Battery Energy Storage Systems (BESSs). In an inverter-dominated microgrid the majority, if not all, of the DERs are interfaced to the microgrid through inverters, i.e., Voltage-Sourced Converters (VSCs).

The control scheme of a microgrid must provide seamless transition between different modes of operation, engage in effective power exchange with the utility in the grid-connected mode, and regulate the microgrid voltage and frequency, i.e., the power quality, in the islanded mode of operation [3].

A microgrid also requires protection systems that ensure its safe operation by locating and isolating internal and external faults in a fast, selective, and reliable manner.

1.2   Statement of the Problem

The proliferation of the highly advantageous microgrid technology has been hindered by the lack of a cost-effective, selective and reliable strategy to protect it against internal and external faults [7]-[9]. The protection strategies proposed in the existing literature either do not apply to the inverter-dominated microgrid or suffer from multiple technical and/or economical issues as discussed in the next section.

Protection system design and verification cannot be performed without an effective control strategy that maintains microgrid stability and provides acceptable dynamic response to disturbances and faults. The existing control strategies that do not rely on communication infrastructure do not meet the aforementioned requirements in the inverter-dominated microgrid.

1.3   Literature Review

This section describes the challenges and requirements of the AC microgrid protection and control and highlights the shortcomings of the existing protection and control strategies.

1.3.1   Microgrid Protection

The protection strategies used in traditional distribution networks are not generally applicable to the inverter-dominated microgrid. This is mainly because the fault response of a microgrid can be drastically different from that of a traditional distribution system [7], [10]. The protection challenges are further complicated in the inverter-dominated microgrid [8], [11], [12]. Conventional Over-Current (OC) relays may fail to detect the limited fault currents contribution from Inverter-Interfaced DERs (IIDERs), especially in the islanded microgrid [6]-[8], [12], [13]. Coordinating OC relays in the inverter-dominated microgrid is also challenging, due to the significantly different fault current levels under the grid-connected and islanded operation modes [6]-[8], [14].

To overcome the aforementioned issues, different microgrid protection strategies have been proposed in the literature. The differential protection strategy [11], [15] is intrinsically more robust against variations of the fault current magnitude. However, a differential relay

requires current measurement at all boundaries of its protection zone [6], [10], which may be costly and impractical in microgrids with multiple feeder sections and geographically dispersed DERs. Besides, differential relays provide unit protection and thus require backup relays utilizing a different protection strategy [6].

Robustness against variations in the fault current levels can be also achieved using adaptive protection schemes [17]-[19]. These schemes require prior knowledge of all possible configurations, operation modes, and the associated fault current levels [16], [10]. The voltage-based protection strategy of [20] is not adversely affected by the varying fault current levels but suffers from lower sensitivity to faults in the grid-connected microgrid [10]. A directional comparison blocking scheme is used in [9] to enable coordination of directional OC relays using dual settings. A common disadvantage of the aforementioned protection strategies is that they all require remote communication which can be prohibitively expensive, especially in large-scale microgrids [6], [10]. Relying on communication networks also increases vulnerability to communication failure and cyber-attacks [16]. Therefore, even if the communication infrastructure is available, there is a need for a backup protection strategy that operates based on locally measured signals.

The literature on microgrid protection also includes non-pilot strategies, i.e., relays that do not require communication signals. Among these, the harmonic measurement method of [8] requires special inverters for fifth harmonic injection and is only applicable to the islanded microgrid. In [21], a wavelet transform-based feature extraction method is combined with a data mining strategy for fault detection and classification in the microgrid. This strategy requires building a data mining model based on a large dataset that contains all possible variations in the microgrid fault behavior, which is usually not practical. The symmetrical component-based protection method of [22] only detects asymmetrical faults [12], [23] and is only applicable to uni-grounded microgrids [24].

The non-pilot directional protection strategies introduced in [11], [12], [23] increase robustness against variations of the fault current magnitude using the definite-time grading technique. However, the protection strategy of [23] and the non-pilot backup protection method of [12] suffer from low sensitivity to resistive ground faults in the islanded inverter-

dominated microgrid. The non-pilot backup protection strategy of [11] utilizes phase OC and negative-sequence OC elements which improve asymmetrical fault detection but would fail to reliably detect symmetrical faults in the islanded inverter-dominated microgrid. In addition, as discussed in Section 3.1.3 and 3.3.1, the traditional phase- and sequence-domain directional elements used in the existing literature fail to accurately determine the asymmetrical fault direction under specific conditions.

1.3.2   Microgrid Control

The control strategies of IIDERs in the microgrid have been extensively discussed in the literature [5], [25]-[27]. The control requirements of DERs do not cause significant complications in the grid-connected operation of the AC microgrid. However, the islanded microgrid requires effective control strategies that enable active and reactive power sharing among the DERs responsible for voltage and frequency regulation, while maintaining stability and acceptable dynamic behavior [28], [29]. To achieve the aforementioned objectives, several power sharing strategies have been proposed in the literature, which are either communication-based or non-communication-based [30]-[37].

Communication-based control strategies include central [30], master-slave [31], average load sharing [32], peak value-based current sharing [33], circular chain [34], and distributed [35] control strategies. The communication-based strategies usually achieve desirable power sharing and voltage/frequency regulation. However, they are more complex, vulnerable to communication failure, and costly. Communication-assisted control methods degrade system reliability, flexibility, modularity and expandability [30]-[35], and thus, are not preferred for large-scale microgrids [28], [29].

The conventional droop control strategy has many advantages such as simple implementation and low cost, as well as high reliability, flexibility, modularity and expandability [36], [37]. However, the conventional droop-based power-sharing strategy suffers from disadvantages such as the trade-off between power sharing accuracy and voltage/frequency deviations, poor dynamic response, and sensitivity to system impedances [36], [37]. To overcome these drawbacks, different variations of droop-based

control strategies have been proposed [28], [29]. For instance, the issue of sensitivity to system parameters can be resolved to a great extent by using the virtual impedance droop-based power-sharing strategy [36], [37]. However, the issue of poor dynamic behavior and disturbance response is still to be fully addressed. A recent study reported in [38] has proposed a Proportional-Derivative (PD) droop control to damp the power oscillations. However, this method results in unacceptable voltage/frequency deviation.

1.4   Research Objectives

The main objectives of this research are (i) developing a selective and reliable non-pilot protection strategy and the associated relay technologies for the inverter-dominated microgrid, (ii) providing a systematic coordination method for the designed relays, and (iii) identifying the most suitable control strategy and making necessary improvements for stable operation of the inverter-dominated microgrid and its acceptable dynamic response to disturbances.

1.5   Methodology

In order to achieve the thesis objectives:

- Off-line time-domain simulation studies are performed in the PSCAD-EMTDC software environment to investigate the transient response of the inverter-dominated microgrid to faults and disturbances.
- The results of the transients studies are utilized to develop protection and control strategies suitable for the inverter-dominated microgrid.
- A comprehensive performance evaluation of the proposed protection and control strategies is realized through off-line time-domain simulation of a realistic study system.
- The proposed protection strategy is implemented in a commercially available relay and evaluated using an industrial relay testing platform.

1.6   Thesis Contributions

In this research (i) an improved droop-based power-sharing strategy is proposed to minimize power oscillations in the islanded microgrid while limiting voltage and frequency deviations, (ii) a new perspective on setting and application of the negative-sequence directional element is introduced. It is explained why the negative-sequence directional element fails in certain cases in an inverter-dominated microgrid and a simple but effective solution is proposed and verified, and (iii) a selective and reliable non-pilot protection strategy for the inverter-dominated microgrid is proposed and verified using simulation studies as well as implementation in a commercially available relay. The proposed protection and control strategies:

- Do not require remote communication.
- Operate satisfactorily under both grid-connected and islanded operating modes without a need for adaptive settings and characteristics of the relays and controllers.
- Are robust against motor starting currents and unbalanced loads.
- Prevent microgrid shut down under grid-side faults.
- Prevent unnecessary tripping of DERs under internal faults.

1.7   Thesis Layout

The next chapters of this thesis are organized as follows:

Chapter 2 introduces the microgrid control systems and proposes an enhanced PD droop controller for power oscillation damping in the inverter-dominated microgrid. The study system used for time-domain transient studies is also introduced in Chapter 2.

Chapter 3 discusses the operating principles of the sequence-based directional elements and how they may fail in an inverter-dominated microgrid. A simple solution is proposed to prevent the aforementioned failure. A non-pilot protection strategy is proposed for the inverter-dominated microgrid, and its selective and reliable operation is verified using extensive fault studies in Chapter 3.

Chapter 4 verifies the practicality of the proposed protection strategy by implementing it in a commercially available relay and investigating its performance using an industrial relay testing platform.

Chapter 5 summarizes the thesis contributions and provides concluding remarks.

Chapter 2

2   Control of the Inverter-Dominated Microgrid

This chapter introduces the IIDER control systems utilized in a typical microgrid, proposes improvements to the conventional droop control strategy, introduces the study system, and verifies the proposed improved droop control strategy through extensive simulation studies performed on the study system under various disturbances.

To investigate the worst-case scenario, it is assumed that all of the DERs are connected to the microgrid through inverters. There is no electrical machine directly connected to the microgrid. Lack of the inherent frequency support provided by machines enables investigation of the worst case scenario in microgrid control, dynamics and stability.

2.1   IIDER Control

This part provides a brief overview of the IIDER structure and control systems of the typical IIDERs. Fig. 2.1 depicts a typical three-phase IIDER that contains a DC energy source, a VSC, an output filter, and an interfacing transformer. The IIDER transfers real and reactive power to or from the grid based on its control objectives.

The VSC control system is extensively discussed in [5], [26], [27], [39]. The control system of a typical IIDER in the dq reference frame includes an inner current control loop, an outer voltage control loop, and the power sharing controller, as shown in Fig. 2.1. The structure of the inner current control loop is usually the same for most inverters. It is responsible for controlling and limiting the terminal current. The outer voltage control loop differs from one IIDER to the other, depending on the type of the energy source and the control objective. Further details are provided in the following sections.

A microgrid should be able to operate in both grid-connected and islanded modes and provide acceptable performance during and after the transition between these two modes of operation. The mode change is detected by the DERs using a passive or active islanding detection method, e.g., the Sandia Frequency Shift (SFS) active islanding detection method [40], [41] which is described in Appendix A.
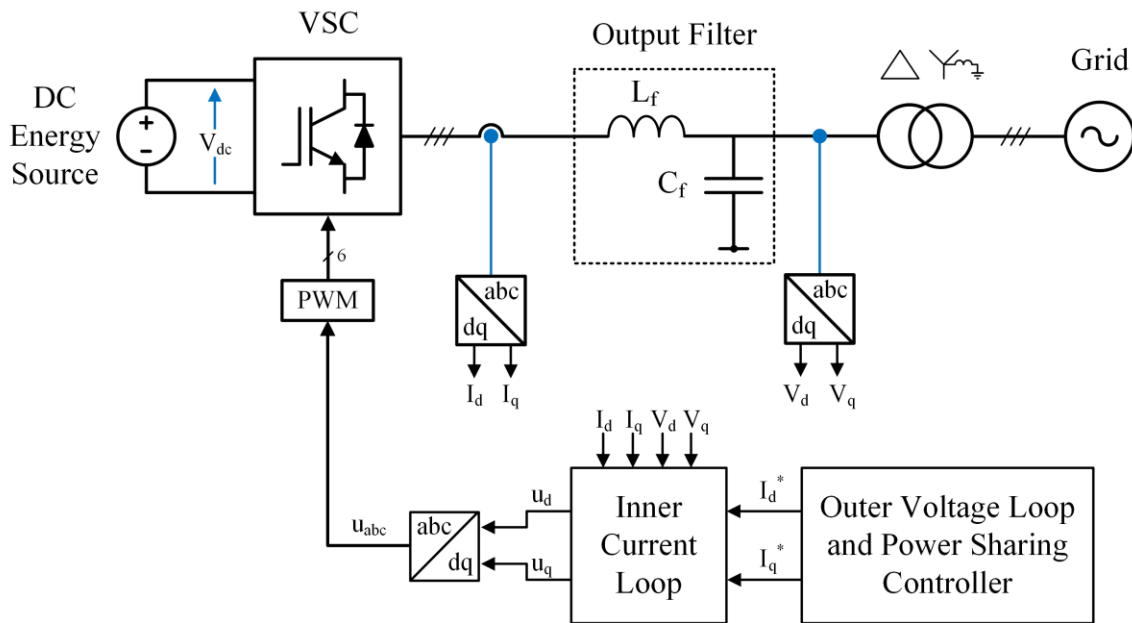
Figure 2.1 Schematic diagram of a typical three-phase IIDER.

In the grid-connected microgrid, the bus voltages and the frequency are imposed by the utility grid and the primary control objective of the DERs is to capture the maximum amount of renewable energy. Therefore, WTs and PV generation systems operate in the Maximum Power Point Tracking (MPPT) mode. In the grid-connected microgrid, BESSs are typically in the charging mode [3]-[5], [42]. If the power generated by the microgrid DERs exceeds the power demands of the loads and BESSs within the microgrid, the excess power is supplied to the grid. Otherwise, additional power is received from the grid [4], [5], [25], [28], [29].

In the islanded mode of operation, microgrid frequency and voltages are usually regulated by BESSs, while WTs and PV generation systems continue to operate in the MPPT mode [4], [5], [25], [28], [29]. However, if the power generation surpasses the power demand, the DGs must operate at a lower capacity and participate in voltage and frequency regulation. On the other hand, when there is not sufficient stored power and generation in the system, the power balance is achieved by shedding non-critical loads.
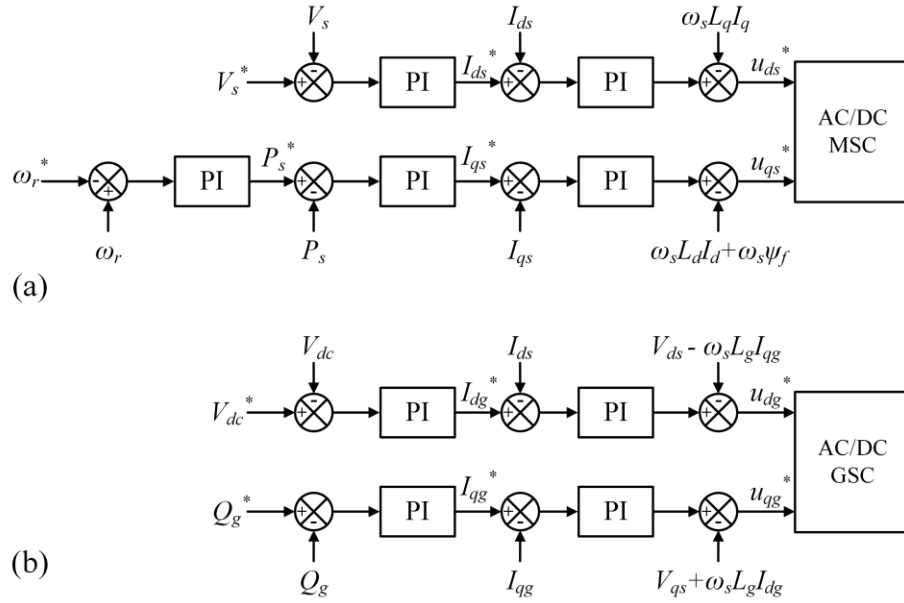
Figure 2.2 Control block diagrams of the PMSG-based WT (a) MSC and (b) GSC.

2.1.1   WT Control

The WTs operate at MPPT mode in both grid-connected and islanded conditions. A Permanent Magnet Synchronous Generator (PMSG)-based WT is considered in this study. The interface system comprises Machine-Side Converter (MSC) and Grid-Side Converter (GSC) controllers. The MSC controls the PMSG active and reactive powers to achieve MPPT and keeps the stator voltage constant at its rated value throughout the entire speed range. The GSC regulates the DC-side voltage and supplies reactive power to the AC-side to meet the grid requirements [43]. The control block diagrams of the MSC and the GSC of the PMSG-based WT are shown in Fig. 2.2 [44], [45].

2.1.2   PV Control

In this study, it is assumed that the PV system operates in MPPT mode in both grid-connected and islanded scenarios. The PV system is interfaced to the AC microgrid through a boost DC/DC converter and a DC/AC VSC, i.e., inverter. The DC/DC converter tracks the maximum power point by controlling the PV array voltage, V_{pv}, as shown in Fig. 2.3 (a). The VSC regulates the DC-link voltage as well as providing reactive power to the AC system to meet the grid requirements [43], Fig. 2.3 (b), [26], [46].
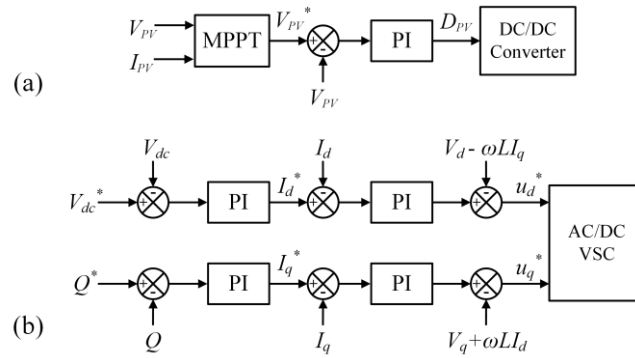
Figure 2.3 Control block diagram of the PV system (a) DC/DC and (b) VSC.
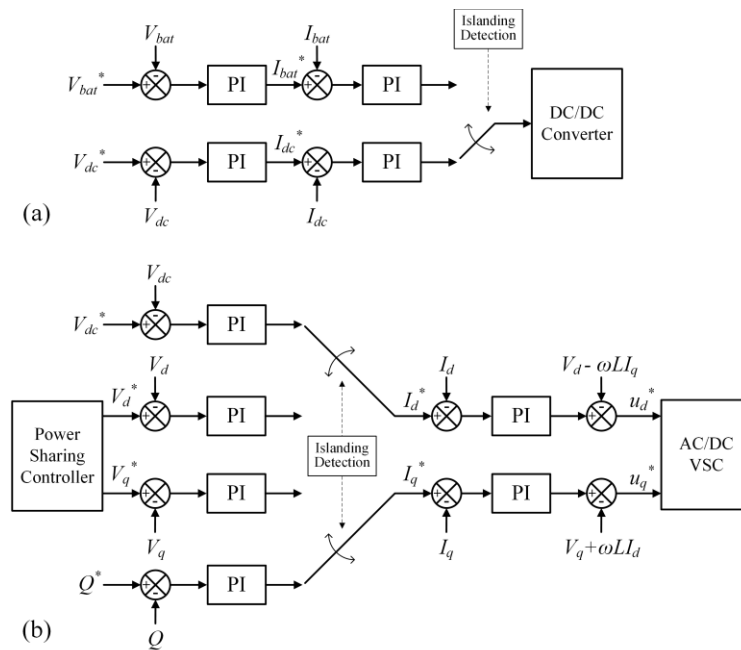
Figure 2.4 Control system of the BESS (a) the DC/DC converter, and (b) the VSC.

2.1.3   BESS Control

The BESS in this study is interfaced to the AC microgrid through a bi-directional DC/DC converter and a VSC. The DC/DC converter controls the battery voltage in the grid-connected mode and regulates the DC-link voltage in the islanded mode, as shown in Fig. 2.4 (a). The VSC controls the DC-link voltage and the reactive power in the grid-connected mode and regulates the AC-side frequency and voltage in the islanded mode, as shown in Fig. 2.4 (b) [47], [48].

2.2   Power Sharing

The stability of the islanded microgrid depends on the collaborative control of the DERs that are responsible for voltage and frequency regulation [25]. In most cases, this task is mainly undertaken by the energy storage system available in the microgrid. The active and reactive power sharing controllers facilitate this collaboration.

In this research, it is assumed that the voltage and frequency regulations are performed by the BESSs. Although the PV and wind units could participate in the regulation, in this study it is assumed that the active capacities of the RESs are assigned to capture the maximum possible energy using MPPT strategies.

BESSs regulate the frequency and the bus voltages in the islanded microgrid by injecting/absorbing active and reactive powers proportional to the frequency and voltage deviations, respectively [4], [5], [28], [29]. In the droop-based control strategy, different energy storage units share this burden in proportion to their power ratings without any communication. This section briefly explains the conventional droop-based control strategy, the PD droop control proposed in [38], and the proposed improved PD droop control strategy.

2.2.1   Conventional Droop Control

The active and reactive powers exchanged by the BESSs that are interfaced to the microgrid through VSCs can be expressed as [4], [5]:

$$P = \frac{V_A}{R^2+X^2}[R(V_A - V_B cos\delta) + XV_B sin\delta] \tag{1}$$

$$Q = \frac{V_A}{R^2+X^2}[-RV_B sin\delta + X(V_A - V_B cos\delta)] \tag{2}$$

where V_A and V_B are the VSC terminal voltage and the microgrid bus voltage, respectively. The angle δ is the phase-angle difference between V_A and V_B. The impedance $Z = R + jX$ is the VSC output impedance, and θ is the impedance angle. In medium voltage microgrids, the impedance Z is mostly inductive. Besides, δ is usually small and thus $sin\,\delta \propto \delta$ and $cos\,\delta \propto 1$. Therefore, (1) and (2) can be simplified as follows [4], [5], [25], [28], [29].
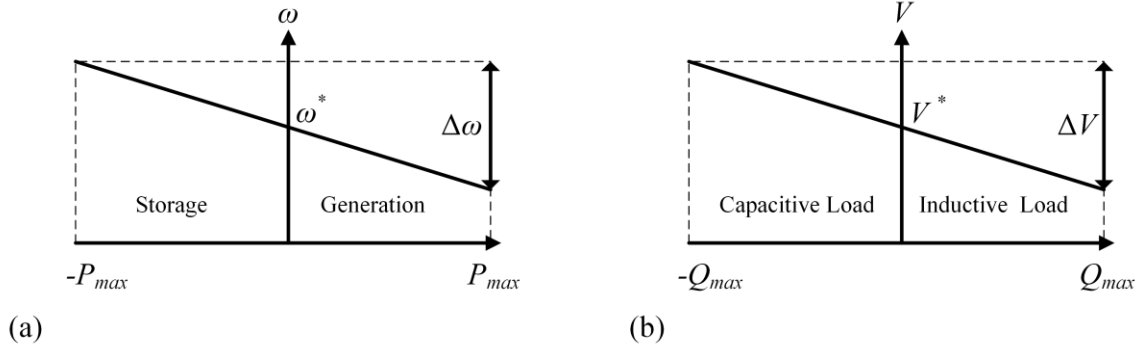
Figure 2.5 (a) frequency droop characteristics, and (b) voltage droop characteristics.

$$P = \frac{V_A V_B}{X} \sin\delta \Rightarrow \delta \propto \frac{XP}{V_A V_B} \tag{3}$$

$$Q = \frac{V_A}{X}(V_A - V_B \cos\delta) \Rightarrow (V_A - V_B) \propto \frac{XQ}{V_A} \tag{4}$$

From (3) and (4), it can be seen that the power angle δ is strongly related to the active power P, and the voltage difference $V_A - V_B$ is strongly related to the reactive power Q. Thus, the VSCs can contribute to the AC-side frequency and voltage regulation by controlling active and reactive power exchange at their AC terminals. Therefore, the droop control characteristics can be expressed as follows [4], [5], [25], [28], [29].

$$\omega - \omega^* = -m(P - P^*) \tag{5}$$

$$V - V^* = -n(Q - Q^*) \tag{6}$$

where ω and V denote the AC-side frequency and voltage, respectively. The corresponding reference values are denoted by ω^* and V^*, respectively. Besides, P and Q represent the active and reactive powers, while their reference values are denoted by P^* and Q^*, respectively. These relationships are shown in the droop characteristics of Fig. 2.5, where m and n denote the slopes of the frequency and voltage droop characteristics, respectively.

The slopes can be selected as follows [4], [5], [25], [28], [29]:

$$m = \Delta\omega / 2P_{max} \tag{7}$$

$$n = \Delta V / 2Q_{max} \tag{8}$$

where $\Delta\omega$ and ΔV are the maximum permitted frequency and voltage deviations and $P_{\max}$ and $Q_{\max}$ are the converter maximum active and reactive powers. Hence, each VSC participates in the frequency and voltage regulation by adjusting its power references according to (7) and (8).

In order to effectively apply the droop control strategy in microgrids with low X/R ratios, e.g., low-voltage microgrids, virtual impedances are introduced by modifying the VSC control system [4], [5], [25], [28], [29]. Using virtual impedances is not necessary in cases where the system X/R ratio is relatively large, e.g., the medium-voltage microgrids investigated in this thesis.

2.2.2 Proportional-Derivative Droop Control

The conventional droop control strategy can cause under-damped power oscillations between the BESSs in the islanded microgrid. To increase damping of the active power oscillations, a PD frequency droop control is introduced in [38] by combining the conventional droop (proportional) controller and a damping (derivative) controller, as follows:

$$\omega = \omega^* - m(P - P^*) - m_d \frac{d(P - P^*)}{dt} \tag{9}$$

A first-order low-pass filter is also added to the derivative term to prevent noise amplification. The resulting PD droop control is implemented as follows:

$$\omega = \omega^* - m(P - P^*) - \frac{m_d S}{S + \omega_c}(P - P^*) \tag{10}$$

where ω_c is the cutoff frequency of the low-pass filter, which is assumed to be 2 rad/s in [38]. A droop gain n_d is also added to the Q–V droop gain n in [38], as shown in (11), with the objective of damping of the reactive power oscillations. The added gain n_d simply increases the total proportional droop gain and does not introduce a derivative term.

$$V = V^* - (n + n_d)(Q - Q^*) \tag{11}$$

2.2.3   Improved Proportional-Derivative Droop Control

It is explained in Section 2.2.2 that adding a derivative term to the conventional droop control, as proposed in [38], considerably increases the damping of power oscillations in the islanded inverter-dominated microgrid. However, the PD droop control strategy adversely affects the frequency regulation in the islanded microgrid. The study results presented in Section 2.2.2 demonstrate that the large time-constant of the low-pass filter in (10), i.e., 0.5 s, leads to unacceptable frequency deviation during the first few seconds after large disturbances. To resolve the increased frequency deviation issue, an improved PD droop control is proposed in this thesis. In the proposed strategy, the PD controller time constant is reduced to 0.01 s, so that it does not cause large and prolonged frequency deviation, without compromising the noise suppression capability.

The added gain n_d in (11) essentially increases the voltage droop gain and thus leads to poor voltage regulation in the steady state, even though the transient response of the system is improved. To resolve this issue, the improved filtered derivative damping transfer function of (10) is also used for voltage oscillation damping, as shown in (12), where a more lenient voltage reference is generated in transient conditions and the steady state operation is not adversely affected.

$$V = V^* - n(Q - Q^*) - \frac{n_d s}{s + \omega_c}(Q - Q^*) \tag{12}$$

The control system block diagram of the proposed improved PD droop control strategy is shown in Fig. 2.6. The performances of the PD droop controller of [38] and the proposed improved PD droop controller are compared in the section 2.2.3 where it is shown that the proposed strategy has a superior performance.
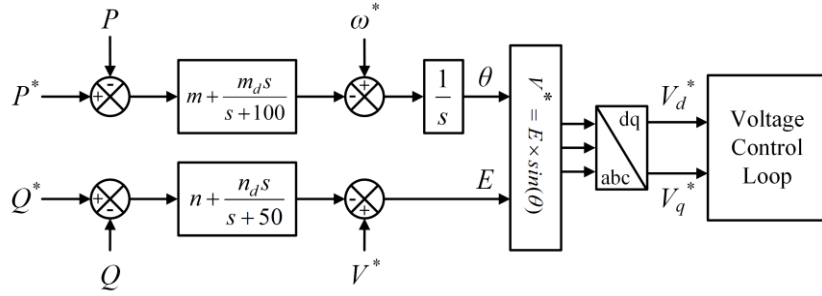
Figure 2.6 Block diagram of the PD droop control with improved active and reactive power oscillation damping.

2.3   Performance Evaluation

In this section, the microgrid response to various disturbances is investigated and the power sharing and voltage regulation performances of the conventional droop, PD droop, and improved PD droop control strategies are compared. In addition, motor starting in the inverter-dominated microgrid is studied and recommendations are made to prevent motor stalling in the islanded mode due to the current limiting characteristics of the IIDERs.

2.3.1   Study System

The simulation studies in this research are conducted using a realistic study system that represents a medium-voltage inverter-dominated microgrid. The study system is developed using detailed models of the microgrid components, e.g., switching-type converters' and the associated control systems. The time-domain transient studies are conducted in the PSCAD/EMTDC software environment. The study system is a modified version of the 27.6 kV Canadian rural distribution network described in [49], which is enabled to operate as a microgrid. Fig. 2.7 shows the single-line diagram of the study system. A 4 MW wind power plant composed of two 2 MW PMSG-based WTs, a 3.5 MW PV generation system, and two 2 MW BESSs are connected to the microgrid at different locations as shown in Fig. 2.7. The study system parameters are provided in Tables I and II of Appendix B. For the simulation studies reported in this chapter, the balanced loads provided in Table III of Appendix B are used.
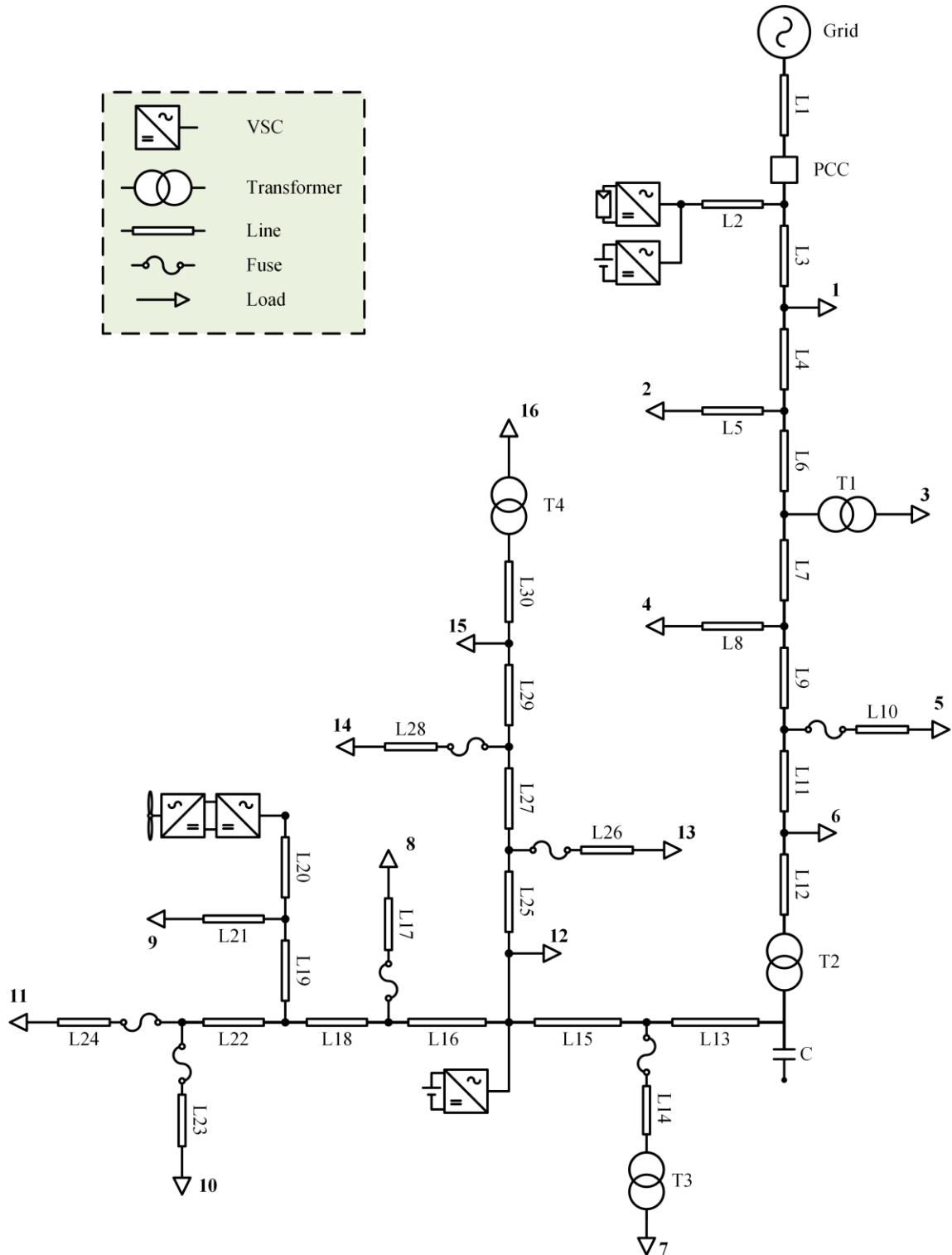
Figure 2.7 Single-line diagram of the study system.

2.3.2   Control Scheme Performance

This part compares the performances of (i) the conventional droop (ii) PD droop, and (iii) improved PD droop control strategies, under a large load disturbance in the islanded microgrid. Table V of Appendix B shows the utilized droop characteristics. To highlight the effects of the utilized frequency droop control strategies on the power oscillations, an equal voltage droop gain of 0.1 per unit is used for all three droop control strategies.

Before the disturbance is applied, the microgrid is in steady-state in the islanded mode. The wind and PV power plants operate at MPPT and generate 4 MW and 3.5 MW with unity power factor, respectively. The BESS1 (BESS2) injects 0.2 MW and 0.6 MVAR (0.2 MW and 0.4 MVAR), to regulate the microgrid frequency and voltage. At $t = 1.1$ s, a significant load disturbance is applied by energizing the Load-16 (2.16 MW and 0.71 MVAR) that brings the total system active and reactive power load to 10.23 MW and 3.2 MVAR, respectively. After $t = 1.1$ s, the active and reactive powers of the BESSs increase to about 1 MW and 0.85 MVAR, respectively.

Due to the inherent lack of inertia in the inverter-dominated microgrid, the BESSs active and reactive powers become oscillatory. This is illustrated in Fig. 2.8. Although the frequency and voltage deviations are not very high, the system behavior is underdamped. Fig. 2.9 shows that the PD droop control strategy mitigated the active and reactive power oscillations. Whereas with the improved PD droop control, shown in Fig 2.11, the active and reactive power oscillations of the BESSs are mitigated faster, and the frequency deviation is lower than that of the PD droop control method. Therefore, the improved PD droop with active power damping control strategy provides increased power oscillation damping while limiting the frequency deviation. The transients behavior is further improved by applying reactive power damping of (12) as seen in Fig. 2.11. As shown in Fig. 2.11(c) the proposed strategy increases the voltage sag after the disturbance by a small amount, i.e., 3 percent, for a short period of time (30 ms). However, this amount is within the acceptable boundaries [43].
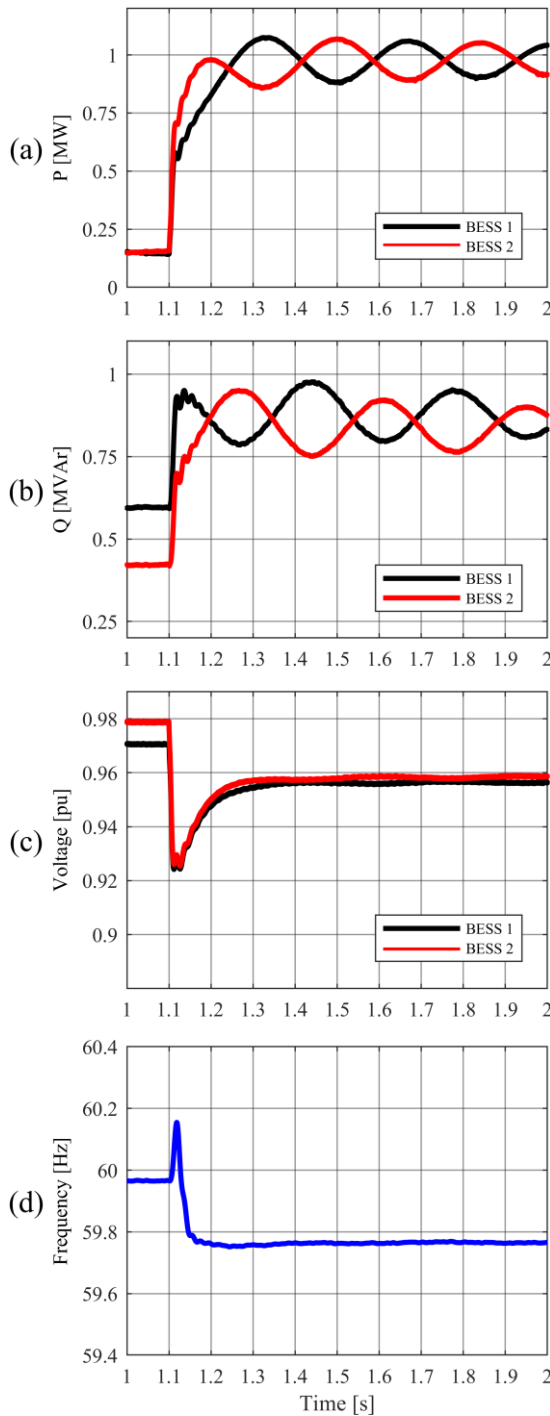
Figure 2.8 Performances of the conventional droop control system after a load disturbance in the islanded mode, (a) active powers, (b) reactive powers, (c) voltage magnitudes and (d) frequency variation.
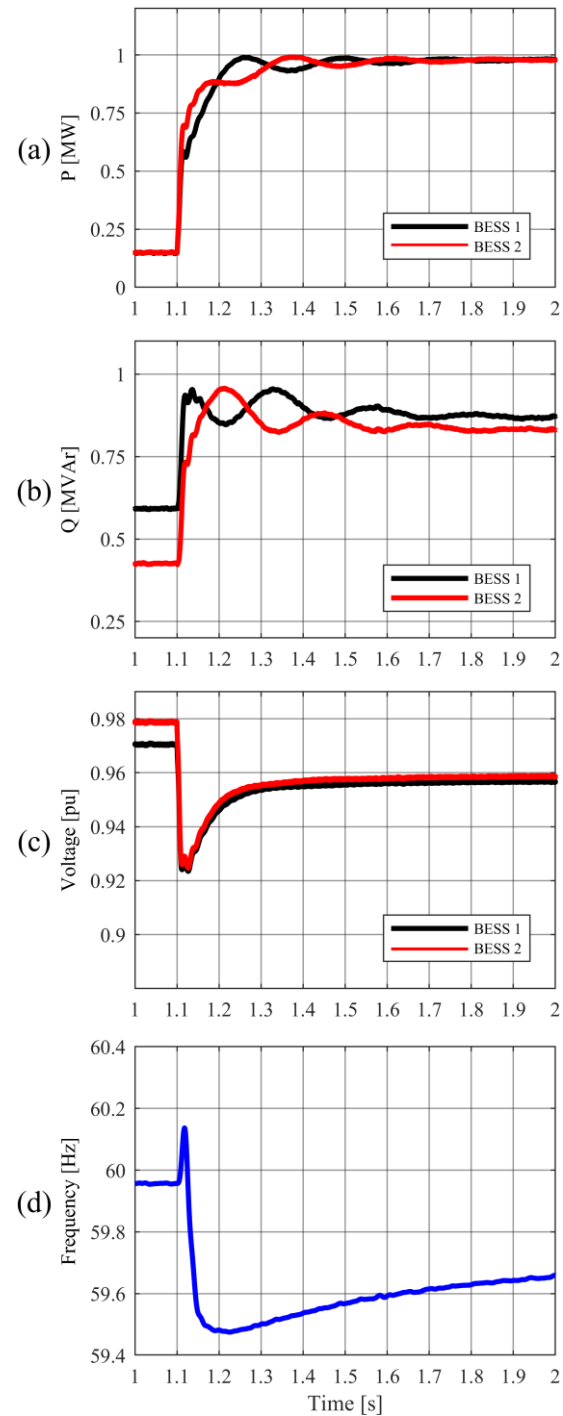
Figure 2.9 Performances of the PD droop control system after a load disturbance in the islanded mode, (a) active powers, (b) reactive powers, (c) voltage magnitudes and (d) frequency variation.
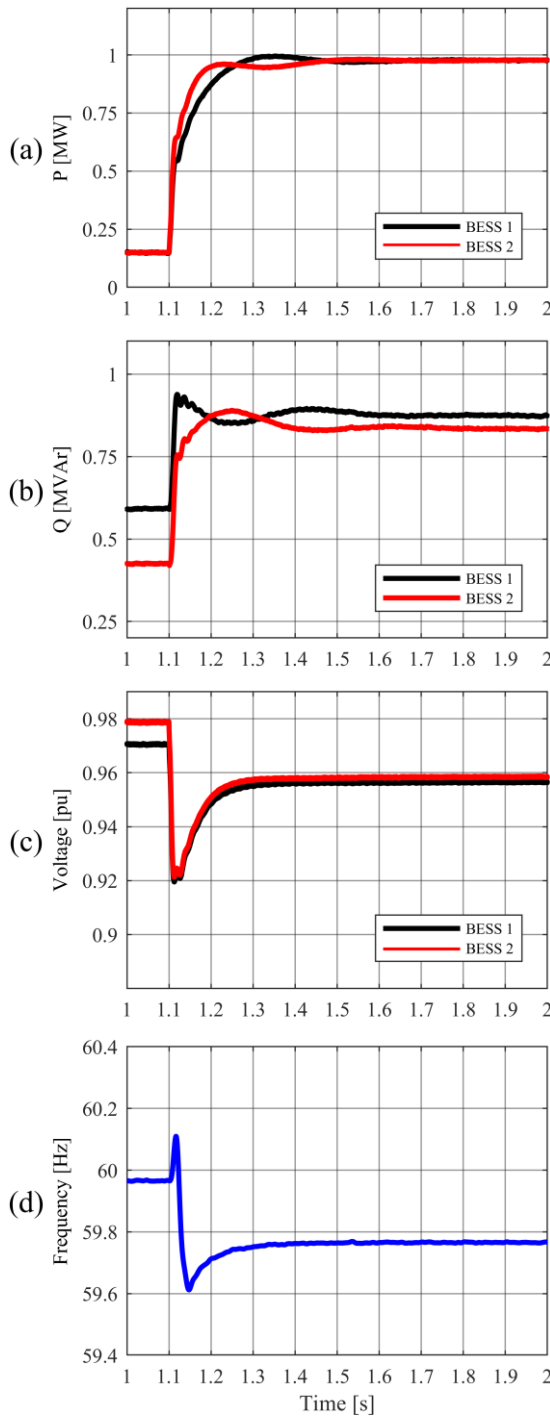
Figure 2.10 Performances of the droop with improved active-power damping control system after a load disturbance in the islanded mode, (a) active powers, (b) reactive powers, (c) voltage magnitudes and (d) frequency variation.
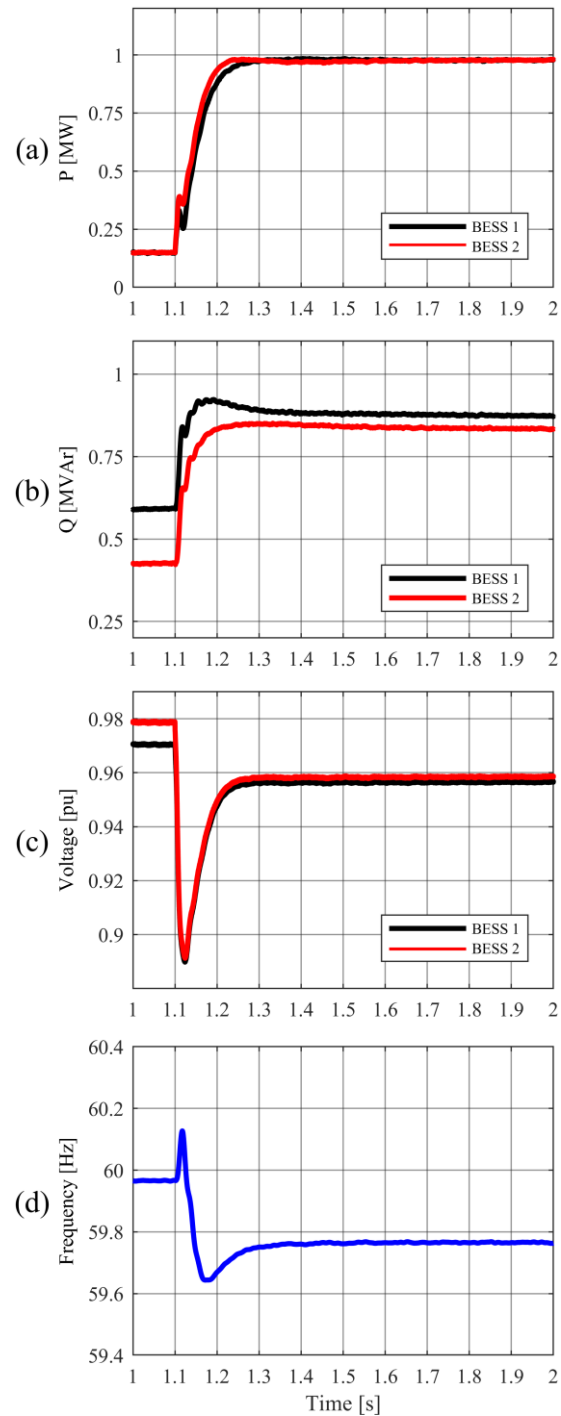
Figure 2.11 Performances of the droop with improved active- and reactive-power damping control system after a load disturbance in the islanded mode, (a) active powers, (b) reactive powers, (c) voltage magnitudes and (d) frequency variation.

2.3.3   Performance under Forced Islanding

Fig. 2.12 shows the performance of the proposed microgrid control strategy, i.e., the improved PD droop control, during a forced islanding scenario and a subsequent load disturbance. The microgrid is in steady-state in the grid-connected mode. At $t = 1.05$ s, a solid phase-to-ground fault occurs in the utility grid. At around $t = 1.14$ $s,$ the microgrid is disconnected from the grid (forced islanding). Due to the power imbalance in the islanded microgrid, the frequency increases until the BESSs detect the islanding condition at around $t = 1.18$ s and change their operation mode to frequency/voltage regulation. Subsequently, the BESSs stabilize the microgrid and regulate the frequency and voltage magnitudes around 60 Hz and 0.95 p.u., respectively. At $t = 1.45$ s, a significant load disturbance is applied to the islanded microgrid and the active power of each BESS increases to about 1 MW to maintain the power balance.

The study results of Fig. 2.12 indicate that the proposed power oscillation damping strategy enables the inverter-dominated microgrid to seamlessly transition from the grid-connected mode to the islanded mode and ride through large load disturbances in the islanded mode.
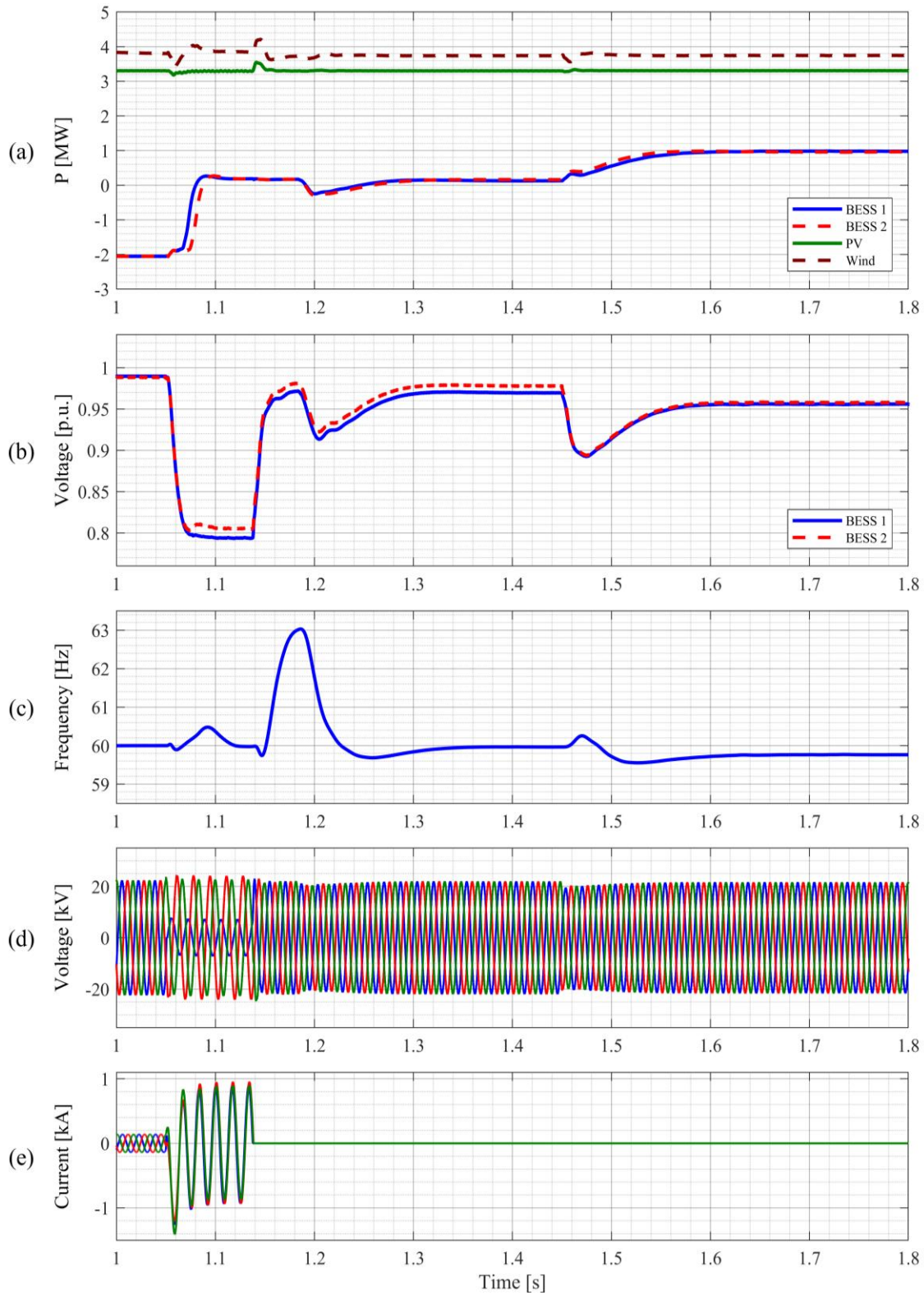
Figure 2.12 Performance of the inverter-dominated microgrid utilizing the proposed improved PD droop controller before and after the transition from grid-connected to islanded mode: (a) active power, (b) positive sequence rms voltage magnitude, (c) frequency, (d) the PCC voltages and (e) the PCC currents.

2.3.4   Motor Starting in the Islanded Microgrid

Induction motors, which are the most common loads in AC distribution systems, consume a significant amount of reactive power during the startup period while increasing their speed. This section investigates the impacts of large startup currents of induction motors on the stability and power quality of the inverter-dominated microgrid and makes recommendations to minimize the associated adverse effects. To illustrate the importance of this issue, a portion of Load-3 in Fig 2.7 is replaced with induction motors, and their startup behavior is investigated. First, a 2 MW motor is energized while the microgrid is in grid-connected mode. This test provides an adequate baseline for comparison with the motor startup in the islanded microgrid.

Fig. 2.13 shows the startup behavior of a 2 MW three-phase motor that is energized at $t = 1.2$ s the motor takes about 1 s to reach its nominal speed and its terminal current during the startup period is about 6 times the rated current. The large reactive current consumed by the induction motor during its startup causes a voltage sag in the microgrid. However, the voltage sag is limited by the reactive power support from the utility grid in the grid-connected microgrid.
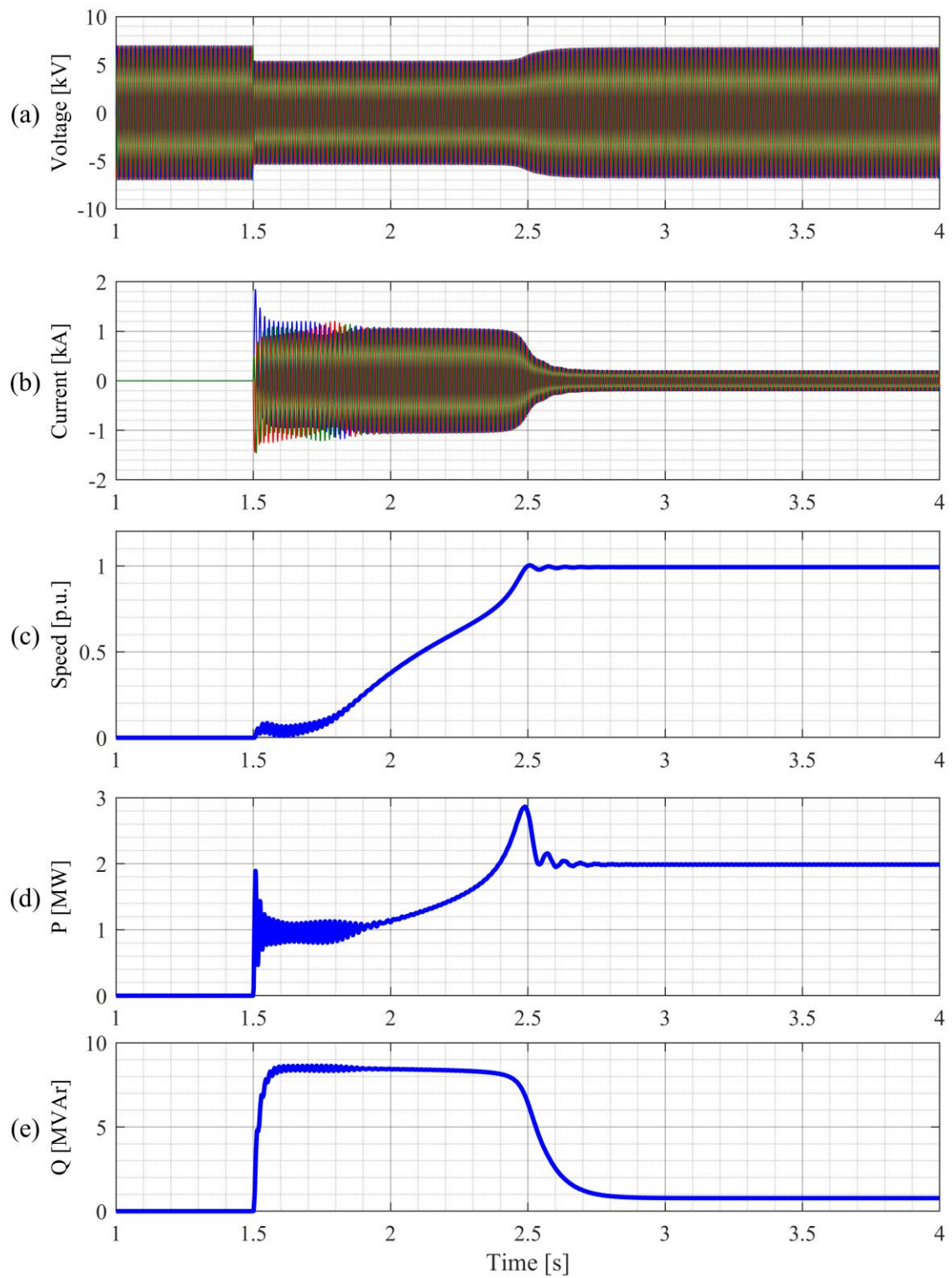
Figure 2.13 Motor startup in grid-connected mode, (a) terminal voltage of the motor, (b) current, (c) motor speed, (d) active power consumed by the motor, and (e) reactive power consumed by the motor.

Fig. 2.14 shows the startup of the same motor in the islanded microgrid where the rest of the loads (8.8 MVA) are of fixed impedance type and generation capacity of 11.5 MVA. The 2.7 MVA excess capacity seems to be sufficient to accommodate a 2MVA load. However, as shown in Fig. 2.14 the IIDERs are unable to provide the increased reactive power consumed by the motor during the startup, and thus the motor fails to start, i.e., stalls. This situation is undesirable as the resulting prolonged voltage sag would damage the motor and other devices in the microgrid.

A rudimentary estimation for the maximum amount of motor load that can be simultaneously energized based on the total and available power in the investigated microgrid can be calculated as follows.

$$I_{DER} = \frac{S_{DER}}{\sqrt{3} \times V} = \frac{11.5 \ MVA}{\sqrt{3} \times 8.31 \ kV} = 0.799 \ kA \tag{13}$$

$$I_{Load} = \frac{S_{Load}}{\sqrt{3} \times V} = \frac{8.8 \ MVA}{\sqrt{3} \times 8.31 \ kV} = 0.611 \ kA \tag{14}$$

$$I_{available} = 1.2 \times I_{DER} - I_{Load} = 0.347 \ kA \tag{15}$$

$$I_{motor} = \frac{S_{motor}}{\sqrt{3} \times V} = \frac{2 \ MVA}{\sqrt{3} \times 8.31 \ kV} = 0.139 \ kA \tag{16}$$

Neglecting the voltage drop in the system, the 6 times the steady state current of 2 MVA induction motor is above the available current in the islanded microgrid, and therefore the motor will fail to start as shown in Fig. 2.14. This study recommends starting motors in the in smaller portions for a faster startup and better power quality in the islanded microgrid. The 2 MVA aggregate motor load can be successfully energized in smaller portions. Fig. 2.15 shows an example of the sequential start of three 0.667 MVA motors. Additionally, the terminal voltage drop is limited to 0.9 p.u. in this case and therefore, the power quality is maintained.
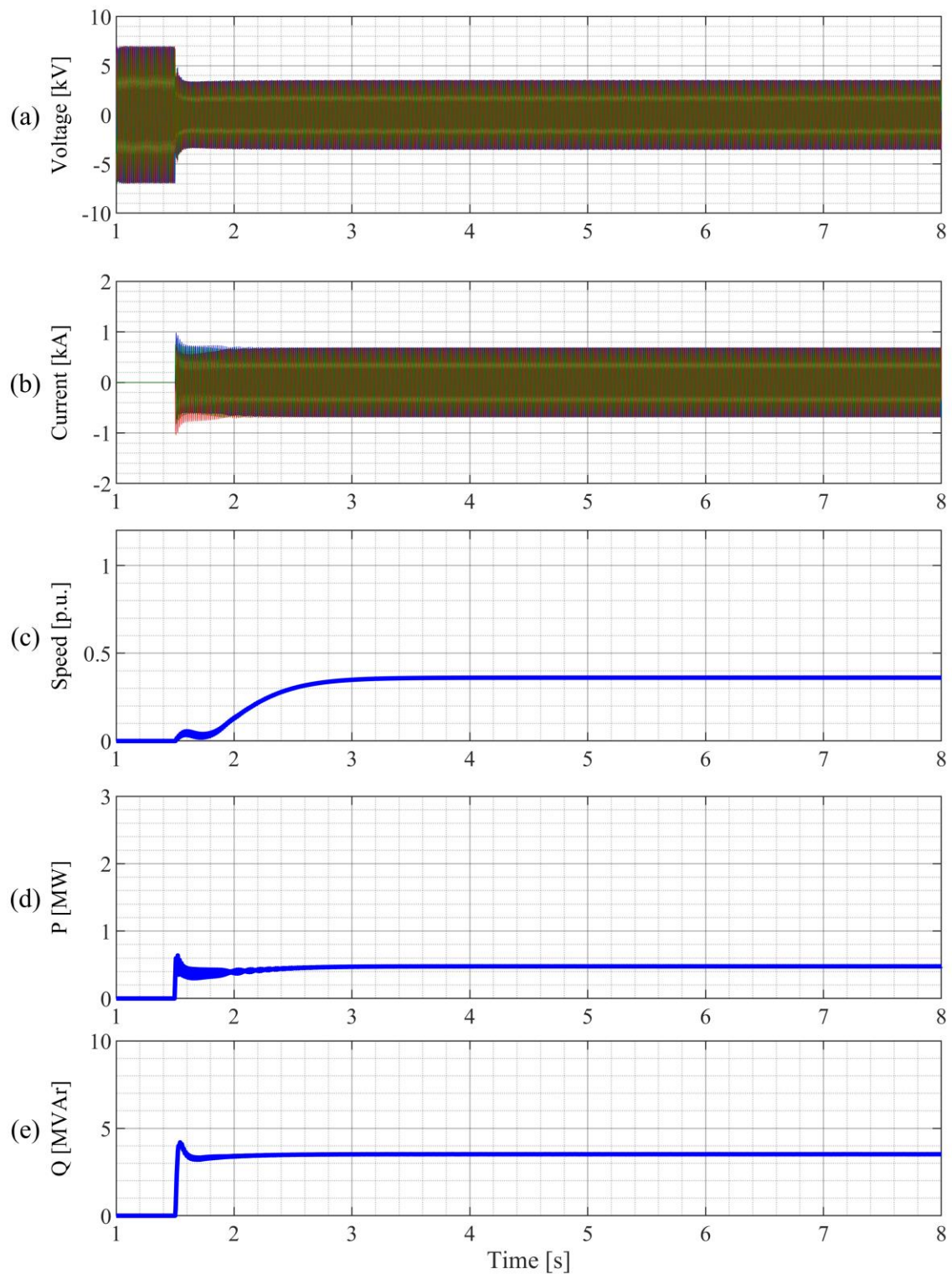
Figure 2.14 Startup of a 2 MW motor in the islanded microgrid, (a) motor terminal voltage, (b) motor terminal current, (c) motor speed, (d) active power consumed by the motor, and (e) reactive power consumed by the motor.
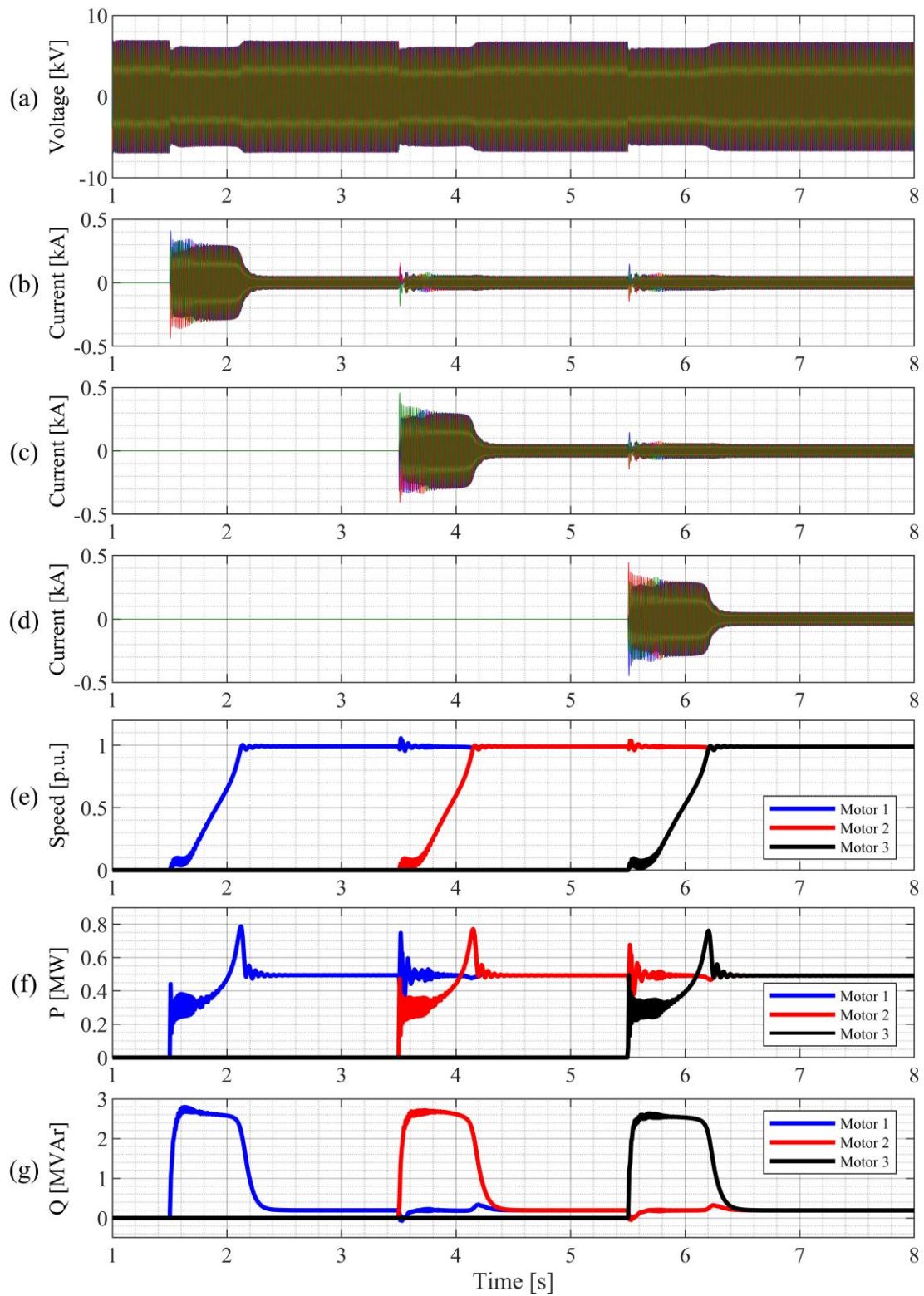
Figure 2.15 Startup of a three 0.667 MW motors in the islanded microgrid, (a) motors terminal voltage, (b) motor 1 terminal current, (c) motor 2 terminal current, (d) motor 2 terminal current, (e) motors speed, (f) active power consumed by the motors, and (g) reactive power consumed by the motors.

2.4   Conclusions

An improved PD droop control strategy is proposed to damp power oscillations between DERs and limit frequency deviations in the islanded inverter-dominated AC microgrid. Power sharing and voltage regulation performances of the conventional droop, PD droop, and improved PD droop control strategies are compared using a detailed and realistic study system simulated in the PSCAD software. The study results indicate that the conventional droop control strategy suffers from under-damped disturbance response, which can cause significant power oscillations during the transition to the islanded mode and after load/generation disturbances in the islanded mode.

Although the PD droop control strategy reduces the active and reactive power oscillations, it increases frequency deviation after large disturbances. Whereas, with the improved PD droop control, the active and reactive power oscillations are more effectively damped while the frequency deviation is smaller than that of the PD droop control strategy. Based on the study results presented in this research, it can be concluded that the proposed improved PD droop control strategy enables effective power sharing and frequency/voltage regulation as well as improving the stability and disturbance response of the inverter-dominated AC microgrid.

Moreover, motor starting and its impact on the islanded microgrid was investigated and sequential starting of motors in the islanded microgrid is recommended for improved power quality and motor protection.

Chapter 3

3   Protection of the Inverter-Dominated Microgrid

Considering the shortcomings of the existing microgrid protection strategies discussed in Section 1.3.1, this chapter introduces a selective and reliable protection strategy for the inverter-dominated microgrid.

The operating principles of the traditional phase- and sequence-domain directional elements are briefly introduced and their advantages and disadvantages are discussed. The reasons that the sequence-domain directional elements may fail to determine the accurate direction of faults in presence of IIDERs are explained. A simple approach is proposed to prevent the aforementioned failures. The improved phase-domain directional elements are used to devise a selective and reliable protection strategy for the inverter-dominated microgrid. The proposed protection strategy is verified using comprehensive fault studies performed on the realistic study system introduced in Section 2.3.1. The proposed protection strategy is also implemented in a commercial relay and its acceptable performance is verified using an industrial relay testing platform.

3.1   Directional Protection Elements

The phase directional element discriminates between forward and reverse faults based on the phase-domain voltages and currents. This element may fail to determine the correct fault direction if the current contains a large zero-sequence component [50], [51]. The shortcomings of the phase directional element have led to the development of sequence directional elements, which usually assess the phase angle differences between the sequence-domain voltages and currents to identify the fault direction. Each of the positive-, negative-, and zero-sequence directional elements determines the directions of specific types of faults more accurately [6], [50].
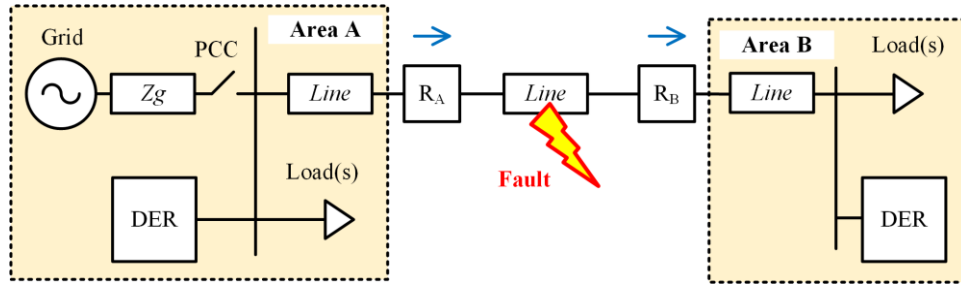
Figure 3.1 A line fault in a typical inverter-dominated microgrid.
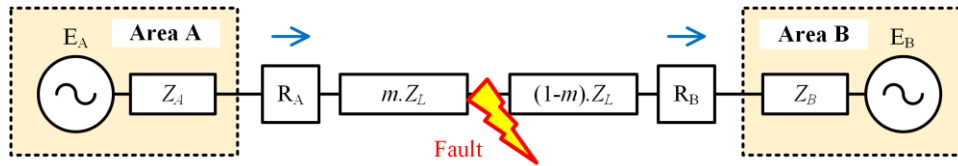
Figure 3.2 Simplified representation of the faulted system of Fig. 3.1.

3.1.1 Symmetrical Faults

The Positive-Sequence Directional Element (PSDE) can be used to determine the directions of symmetrical faults [6], [50], [52]. Assume a symmetrical fault happens on a line connecting two areas of a microgrid, Fig. 3.1, where the per-unit distance to the fault is denoted by $0 \leq m \leq 1$. Each of the areas A and B may contain sources, loads, lines, and the PCC with the utility grid.

Representing these areas with the associated Thevenin equivalent circuits results in the simplified, yet accurate, circuit diagram of Fig. 3.2. Assume the relays at the two ends of the faulted line, i.e., R_A and R_B, utilize PSDEs with the reference directions shown in Fig. 3.2.

The positive-sequence network corresponding to the symmetrical fault scenario is shown in Fig. 3.3, where the subscript 1 identifies the positive-sequence quantities and parameters.
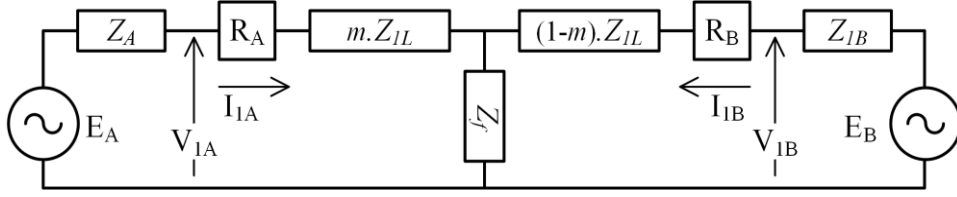
Figure 3.3 Positive-sequence network corresponding to the faulted microgrid of Fig. 3.1, when the fault is symmetrical.

The positive-sequence voltage phasors measured by R_A and R_B are defined by (1) and (2), respectively.

$$V_{R_A} = V_{1A} = m \times Z_{1L} \times I_{1A} + Z_f \times (I_{1A} + I_{1B}) \tag{1}$$

$$V_{R_B} = V_{1B} = (1-m) \times Z_{1L} \times I_{1B} + Z_f \times (I_{1A} + I_{1B}) \tag{2}$$

Neglecting the impact of the fault impedance ($Z_f \approx 0$), the approximate positive-sequence current seen by R_A and R_B are:

$$I_{R_A} = I_{1A} \approx \frac{V_{1A}}{m \times Z_{1L}} \tag{3}$$

$$I_{R_B} = -I_{1B} \approx -\frac{V_{1B}}{(1-m) \times Z_{1L}} \tag{4}$$

The PSDEs of R_A and R_B measure the following angles [52]:

$$\angle V_{R_A} - \angle I_{R_A} = \angle(m \times Z_{1L}) = \angle Z_{1L} \tag{5}$$

$$\angle V_{R_B} - \angle I_{R_B} = \angle(-(1-m) \times Z_{1L}) = \angle - Z_{1L} \tag{6}$$

Thus, there is approximately 180 degrees difference between the angles of the positive-sequence impedances seen by a relay, under forward and reverse symmetrical faults. This large difference is used by the PSDE to reliably determine the fault direction [52]. The fault is assumed to be in the forward direction if the measured positive-sequence impedance angle falls in a half-plane of ±90 degrees around the Element Characteristics Angle (ECA), which is typically set at $\angle Z_{1L}$ to maximize the security margin [50], [52].
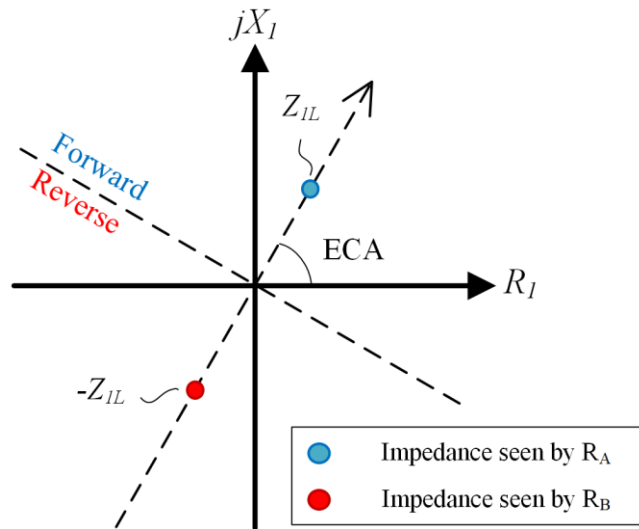
Figure 3.4 Operating characteristics of the PSDE and the positive-sequence impedances seen by R_A and R_B when the fault of Fig. 3.1 is symmetrical.

Fig. 3.4 shows the operating characteristics of the PSDE as well as the sequence impedances measured by this protective element, under forward and reverse fault.

However, it is reported in [6], [51]-[53] that setting the ECA at $\angle Z_{1L}$ may cause false determination of the symmetrical fault direction in systems with high penetration of DERs, due to the associated reactive power injection. To prevent such issues, setting the ECA of the PSDE at values smaller than the $\angle Z_{1L}$ is proposed in [52] and [53].

3.1.2   Asymmetrical Faults

The Zero-Sequence Directional Element (ZSDE) and the Negative-Sequence Directional Element (NSDE) have been widely used to determine asymmetrical fault direction [6], [50], [51]. The ZSDE (i) does not identify the directions of phase-to-phase faults, (ii) has different design requirements depending on the system grounding strategy [6], [54], which drastically varies between different microgrids [24], (iii) is prone to failure due to zero-sequence mutual coupling, and (iv) requires substation transformer neutral current measurement or broken delta-connected voltage transformers [54]. The NSDE does not suffer from the aforementioned issues [6], [50], [51], [54]. Therefore, the rest of this section is focused on the operating principles and application challenges of the NSDE.
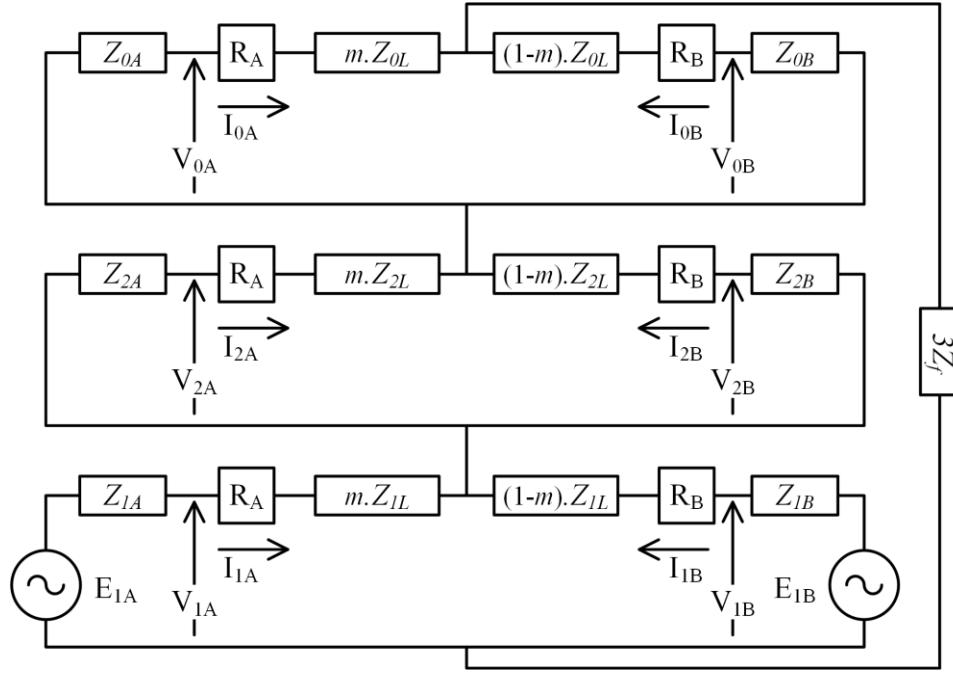
Figure 3.5 Sequence network corresponding to the fault scenario of Fig. 3.1, when the fault is of SLG type.

Assume the fault of Fig. 3.1 is asymmetrical and of Single Line-to-Ground (SLG) type. The sequence network corresponding to this fault scenario is shown in Fig. 3.5, where the subscripts 0, 1, and 2 identify the zero-, positive-, and negative-sequence quantities and parameters [50], [54], [55].

In Fig. 3.5, the areas A and B are represented by the corresponding Thevenin equivalent circuits in the sequence domain. Assume the relays at the two ends of the faulted line, i.e., R_A and R_B, utilize NSDEs with the reference directions shown in Fig. 3.2. The negative-sequence voltage phasors measured by R_A and R_B are defined by (7) and (8), respectively [50], [52], [55].

$$V_{R_A} = V_{2A} = -Z_{2A} \times I_{2A} \tag{7}$$

$$V_{R_B} = V_{2B} = -Z_{2B} \times I_{2B} \tag{8}$$

The impedances Z_{2A} and Z_{2B} are the Thevenin equivalent negative-sequence impedances of the systems interconnected by the faulted line, hereafter referred to as the system negative-sequence impedances. By analyzing the sequence diagrams associated with Line-to-Line (LL) and Line-to-Line-to-Ground (LLG) faults, it can be shown that (7) and (8)
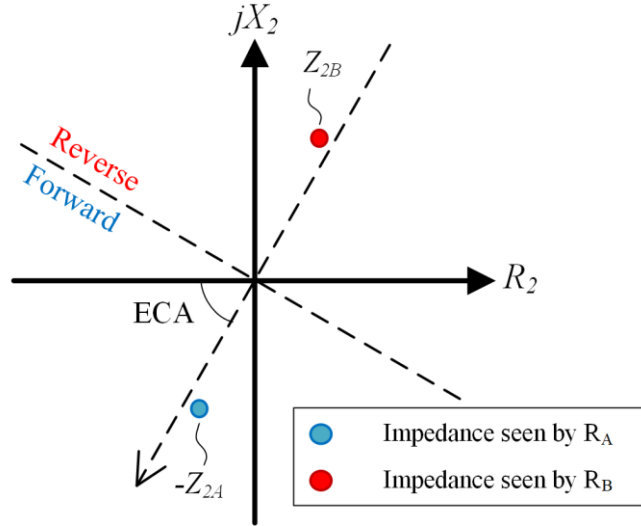
Figure 3.6 Operating characteristics of the NSDE and the negative-sequence impedances seen by R$_A$ and R$_B$ when the fault of Fig. 3.1 is asymmetrical.

apply to all asymmetrical faults [11]. The negative-sequence currents measured by R$_A$ and R$_B$ are $I_{R_A} = I_{2A}$ and $I_{R_B} = -I_{2B}$, respectively. Thus, if the fault of Fig. 3.1 is asymmetrical, the NSDEs of R$_A$ and R$_B$ measure the following impedance angles:

$$\angle V_{R_A} - \angle I_{R_A} = \angle(-Z_{2A}) \tag{9}$$

$$\angle V_{R_B} - \angle I_{R_B} = \pi + \angle(-Z_{2B}) = \angle Z_{2B} \tag{10}$$

The impedances Z_{2A} and Z_{2B} are not fixed and usually not accurately known. However, in traditional transmission systems and legacy distribution networks that are not dominated by inverters, these are typically resistive-inductive impedances with angles close to the line impedance angle $\angle Z_{1L}$. Therefore, the operating characteristic of the NSDE is similar to that of the PSDE, except the directional logic of the NSDE is inverted. Whenever the measured negative-sequence impedance is aligned with the $\angle Z_{1L}$, a reverse direction is detected by the NSDE and vice versa [50], [55]. Fig. 3.6 shows the operating characteristics of the NSDE as well as the sequence impedances measured by this protective element, under forward and reverse faults.

The ECA of the NSDE is conventionally set at $\angle Z_{1L}$, based on a few assumptions that are only valid in traditional power systems. It has been reported that the NSDE may fail to determine the correct asymmetrical fault direction in the presence of IIDERs [6], [51], [56]. The next part investigates this issue and proposes a simple but effective solution.

3.1.3   New Perspective in Setting and Application of the NSDE

The practice of setting the ECA of the NSDE at $\angle Z_{1L}$ was initially adopted to maximize the operating torque produced in electromechanical relays. This is the reason that the ECA is also referred to as the Maximum Torque Angle (MTA) [50], [52]. The same strategy is still used in setting modern digital relays, assuming that the angles of the system negative-sequence impedances, i.e., $\angle Z_{2A}$ and $\angle Z_{2A}$ in Fig. 3.5, are close to the line impedance angle $\angle Z_{1L}$. This assumption is not necessarily valid in an inverter-dominated microgrid where the angle of the system negative-sequence impedance depends on the control strategies of the IIDERs.

Under asymmetrical faults, IIDERs exchange different amounts of negative-sequence reactive current with their host systems, depending on their control and current limiting strategies [13], [14], [57]-[61]. It is shown in [57] that IIDERs operating based on the voltage support control strategy, which are needed in the islanded microgrid, can inject considerable amounts of negative-sequence reactive current into the faulted host system. Besides, the studies reported in [14] indicate that IIDERs operating based on the constant power and constant current control strategies, including those that aim to suppress the negative-sequence current, inject small amounts of negative-sequence reactive current to the faulted host system, due to their harmonic filter capacitors. The reactive behavior of IIDERs in the negative-sequence domain can change the impedance angles seen by NSDEs and cause their malfunction.

Fig. 3.7 shows the potential impact of the negative-sequence reactive current injected by the IIDERs in Area B on the impedance measured by the NSDE of R$_B$ when the fault of Fig. 3.1 is asymmetrical. As shown in Fig. 3.7, depending on the sizes, types, and locations of the IIDERs, the resulting shift in the measured negative-sequence impedance can even
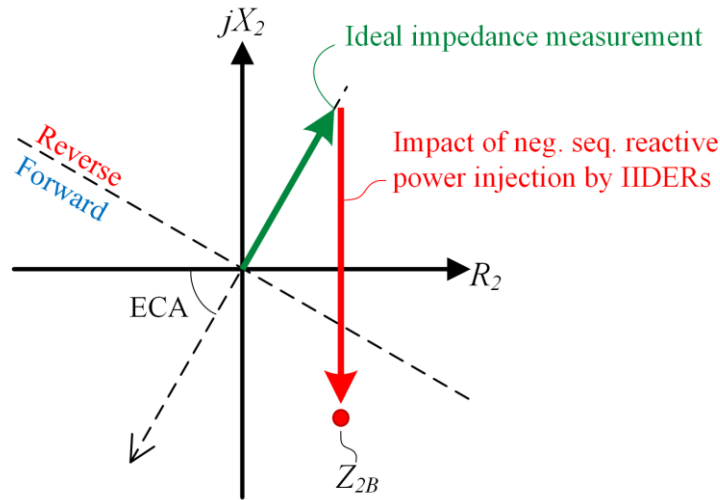
Figure 3.7 Impact of the negative-sequence reactive power injection by IIDERs on the impedance measured by the NSDE during a reverse asymmetrical fault.

cause the NSDE to see a reverse fault as a forward fault if the ECA is set at $\angle Z_{1L}$. The relay R_A could experience similar issues during asymmetrical faults in the islanded microgrid where the strong grid no longer exists and the negative-sequence behavior of the IIDERs in area A become more impactful.

Malfunction of NSDEs due to the impacts of IIDERs has been reported in [56], which confirms the above analysis. Using a smaller non-zero ECA is recommended in [56] to avoid the aforementioned issues. In order to maximize the reliabilities of the PSDE and the NSDE, this research proposes setting the associated ECAs at zero degrees. This results in complete desensitization of these sequence-domain directional elements to the reactive components of the positive- and negative-sequence currents without requiring new algorithms or hardware. The necessity and effectiveness of the proposed solution are verified in Section 3.3.1 using comprehensive fault studies performed on a realistic microgrid study system.

3.2   Proposed Protection Strategy

The non-pilot protection strategies of [11], [12], [23] utilize an Interface Protection Relay (IPR) at the PCC and multiple Microgrid Protection Relays (MPR) along the feeder(s). In this section, improved IPR and MPR algorithms are proposed for the protection of the inverter-dominated microgrid. The proposed relays utilize a combination of phase- and

sequence-domain elements to reliably detect the occurrence of symmetrical and asymmetrical faults. Besides, the directions of symmetrical and asymmetrical faults are determined using the improved sequence-domain directional elements described in Section 3.1.

The fault current magnitude in an islanded inverter-dominated microgrid does not considerably depend on the fault location. The reason is that the fault current is mainly dictated by the current limits of the inverters [14] and not the fault loop impedance. Hence, the traditional time-current (inverse-time OC) grading strategy does not guarantee coordinated operation of non-pilot protective devices in the inverter-dominated microgrid. The proposed protection strategy is based on the definite-time grading technique of [11], [12], [23].

3.2.1   Interface Protection Relay

The IPR must discriminate between internal and external faults and trip the PCC circuit breaker in a timely manner, whenever a fault is detected. The fault detection criteria and the tripping delay of the proposed IPR are different for internal (forward) and external (reverse) faults [52], as explained below.

3.2.1.1   Protection Against Symmetrical Faults

Under internal symmetrical faults, the fault current contribution from the grid is expected to be relatively large for all three phases [12]. Hence, the forward-direction symmetrical fault timer of the IPR starts once (i) a symmetrical fault is detected using three instantaneous phase OC elements, and (ii) a forward fault direction is detected by the PSDE with the zero ECA setting as described in Section 3.1. The pickup setting of the OC elements, I_{P-PU}, is set at a value that is higher than (i) two times of the maximum balanced load current seen by the IPR under normal operating conditions and (ii) the maximum expected motor starting current seen by the IPR. The IPR trips whenever the timer reaches the fixed pre-set threshold TD_{fwd}.

The response of the inverter-dominated microgrid to external symmetrical faults is drastically different. Due to the limited fault current contributions of the IIDERs, the IPR has to detect external symmetrical faults using UV elements rather than OC elements. False

tripping of dead lines is prevented using a load current detection module consisting of three phase-overcurrent elements with a small pickup current. Hence, the reverse symmetrical fault timer of the IPR starts once (i) a symmetrical fault is detected using three instantaneous phase UV elements endorsed by the load current detection module, and (iii) a reverse fault direction is detected by the PSDE. The pickup setting of the UV element, $V_{P\text{-}PU}$, is set at 50 percent of the rated voltage. The IPR trips whenever the timer reaches the pre-set threshold TD_{rev}.

3.2.1.2   Protection Against Asymmetrical Faults

The IPR detects the occurrence of asymmetrical faults mainly using a negative-sequence OC element [11], [22], [62]. This element does not react to balanced load currents and therefore can use a small pickup setting [62], [63]. To further increase sensitivity of the IPR to asymmetrical faults with large fault resistances, a negative-sequence Over-Voltage (OV) element is also added to the fault detection algorithm. The IPR determines the asymmetrical fault direction using the NSDE with the zero ECA setting as described in Section 3.1. The forward (reverse) asymmetrical fault timer of the IPR starts once (i) an asymmetrical fault is detected, and (ii) a forward (reverse) faults is indicated by the NSDE.

The pickup setting of the OC element, $I_{2\text{-}PU}$, is set at twice the maximum negative-sequence current caused by unbalanced loads under normal operating condition. The pickup setting of the OV elements, $V_{2\text{-}PU}$, is set at a value higher than twice the maximum expected negative-sequence voltage caused by unbalanced loads under normal operating condition. The IPR trips whenever the forward (reverse) fault timer reaches the fixed pre-set threshold of TD_{fwd} (TD_{rev}). Fig. 3.8 shows the logic diagram of the proposed IPR.
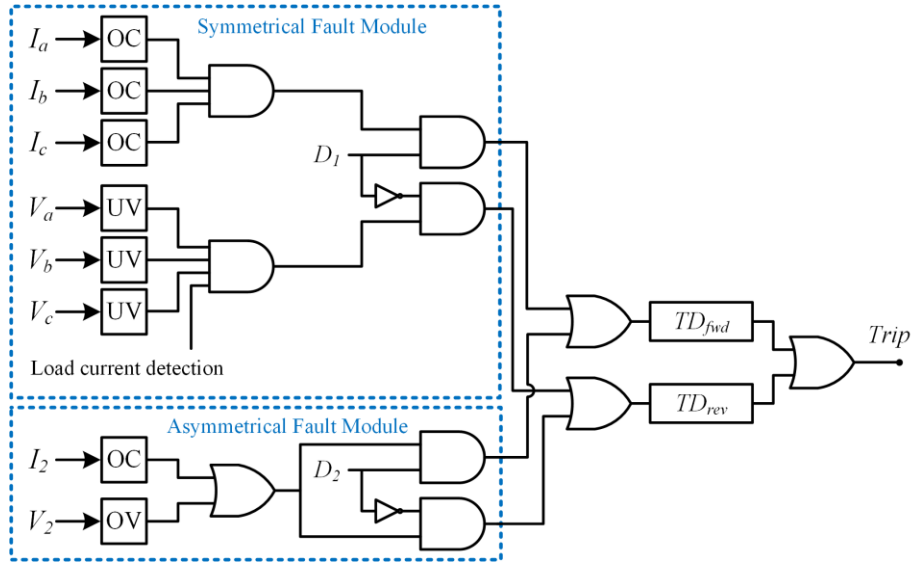
Figure 3.8 Logic diagram of the proposed IPR.

3.2.2 Microgrid Protection Relays

The MPR is expected to detect the occurrence and direction of any symmetrical or asymmetrical fault and operate in coordination with the other protective devices. Due to the reasons explained in 3.2.3, the proposed protection strategy islands the microgrid under any fault, before the first MPR trips. Symmetrical faults in the islanded inverter-dominated microgrid cause the phase voltage magnitudes to drop significantly. Therefore, each MPR detects the occurrence of symmetrical faults using instantaneous phase UV elements. The forward (reverse) fault timer of each MPR starts once (i) a symmetrical fault is detected, and (ii) a forward (reverse) fault direction is indicated by the PSDE. The MPR trips whenever the forward (reverse) fault timer reaches the fixed pre-set threshold of TD_{fwd} (TD_{rev}). The pickup setting of the phase UV elements, V_{P-PU}, is set at 50 percent of the rated voltage. For passive feeders, i.e., feeders without DERs, phase OC elements are added to the fault detection logic to prevent false tripping under faults on adjacent feeders [23]. The asymmetrical fault detection algorithm of the MPR is identical to that of the IPR. Fig. 3.9 shows the logic diagram of the proposed MPR.
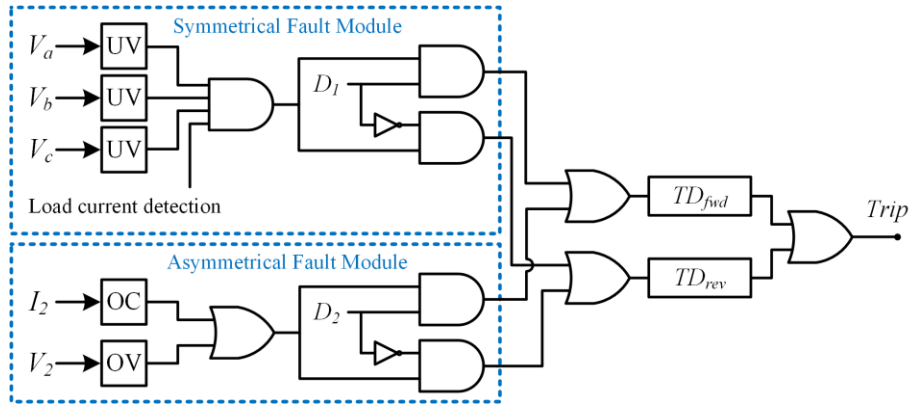
Figure 3.9 Logic diagram of the proposed MPR.

3.2.3   Protection Coordination

Selective protection of the inverter-dominated microgrid is achieved through coordinated operation of the lateral fuses, the IPR, and the MPRs. Under external faults, the IPR is expected to trip as fast as possible, without intentionally delaying its operation for coordination with other protective devices. This strategy prevents exposure of the microgrid components to prolonged voltage sags caused by utility grid faults, and also minimizes the risk of unintentionally islanding a portion of the utility grid (energizing external faults) for an extended period of time. However, to prevent unwanted tripping of the IPR due to system transients, induced voltages, etc., the short delay of $TD_{rev} = 50$ ms is used in the symmetrical and asymmetrical fault modules of Fig. 3.8.

Under internal faults, the IPR must trip the PCC circuit breaker adequately fast, in order to minimize exposure of the microgrid components to large fault currents. However, instantaneous tripping of the IPR would prevent lateral fuses within the microgrid from clearing downstream faults, due to the subsequent drop in the fault current magnitude. When an internal fault takes place, the upstream fuse is the first protective element to react to the fault, if the faulted circuit is protected by a fuse. Thereafter, the IPR causes forced islanding. To provide the fuses with sufficient fault clearing time, the IPR utilizes a fixed and relatively short forward fault delay TD_{fwd} for both symmetrical and asymmetrical faults.
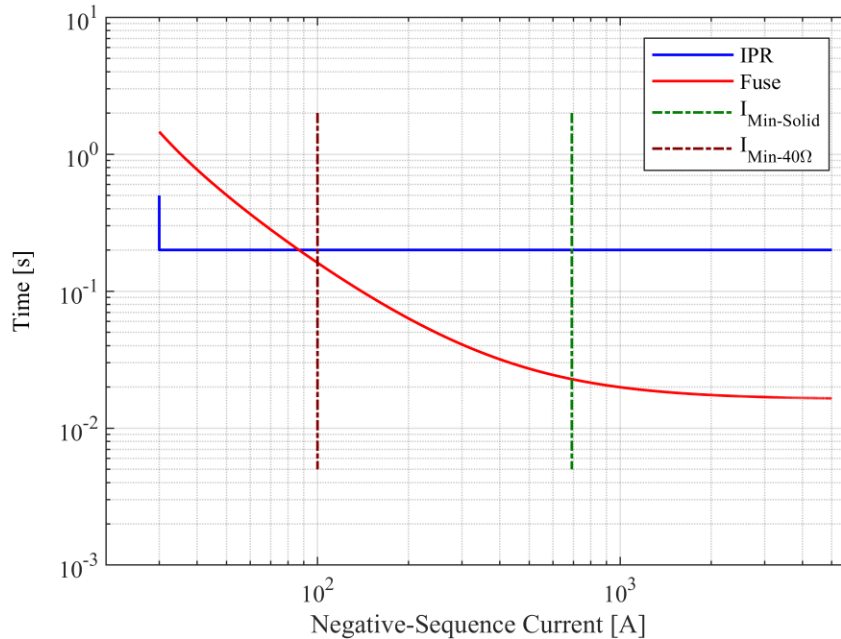
Figure 3.10. IPR-fuse coordination for asymmetrical faults.

The delay is larger than the maximum Total Clearing Time (TCT) of all fuses within the microgrid. The aforementioned maximum TCT is determined by applying SLG faults to all fuse-protected laterals, with a reasonably large fault resistance, which is assumed to be 40 Ω [64]. The coordination is shown in Fig. 3.10 where the operation time, i.e., TCT, of the fuse for faults with impedance smaller than 40 Ω is shorter than of the IPR.

After islanding, the MPRs operate in coordination with each other to selectively isolate the faulted feeder section, if the internal fault is not cleared by any fuse. The Coordination Time Interval (CTI) which is utilized to maintain sufficient operating time delay margin between distribution system relays is typically in the range of 0.2 to 0.5 s [9], [54]. In this study, all relays are coordinated with each other by a CTI of 0.2 s.

3.3   Study Results

This section presents the results of time-domain simulation studies performed on an inverter-dominated microgrid study system in the PSCAD/EMTDC software environment. The study system is developed by modifying the rural distribution system of [49] to enable its operation as a microgrid. Fig. 3.11 shows the single-line diagram of the study system.
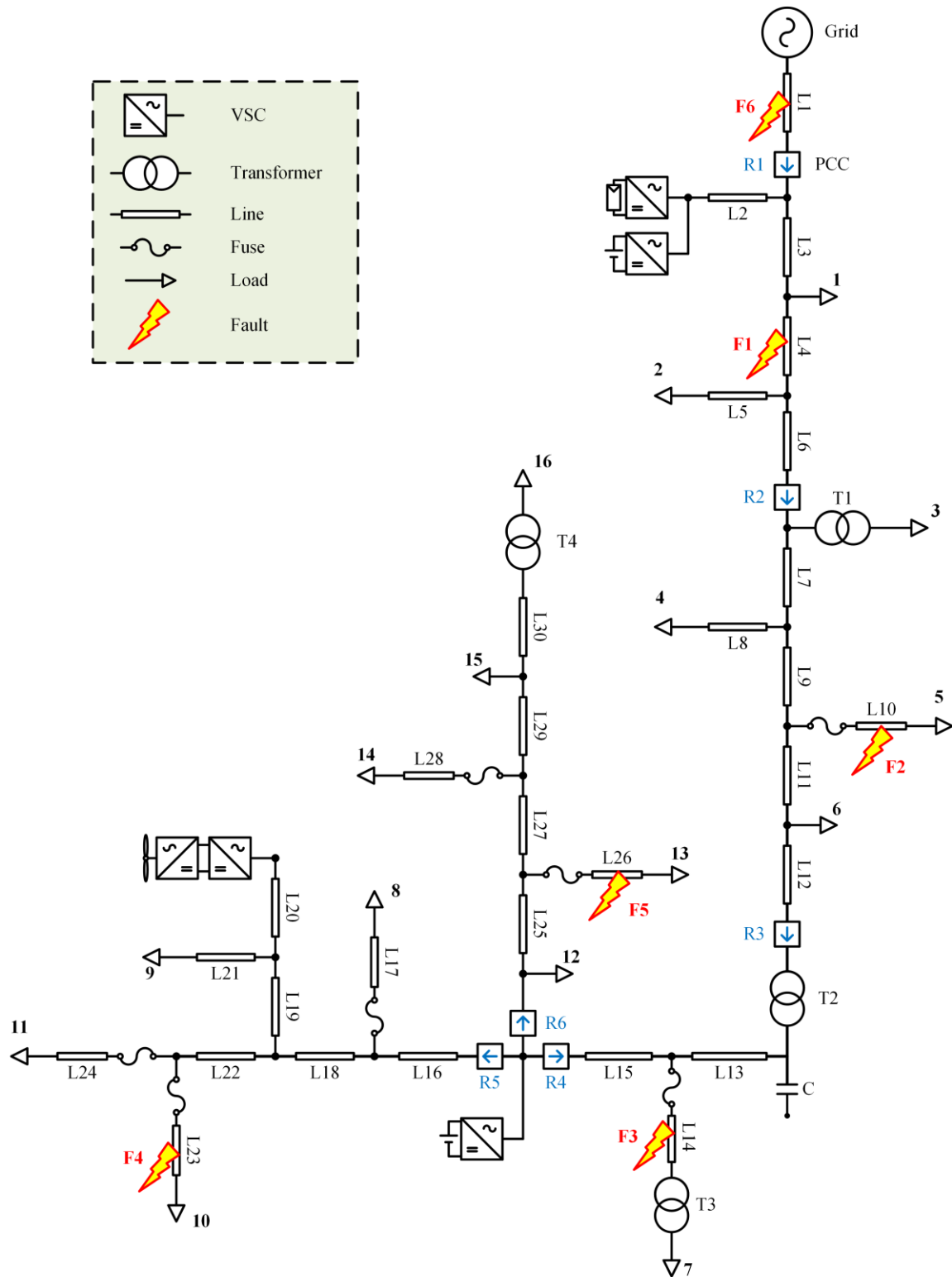
Figure 3.11. Single-line diagram of the study system with the location of faults and relays.
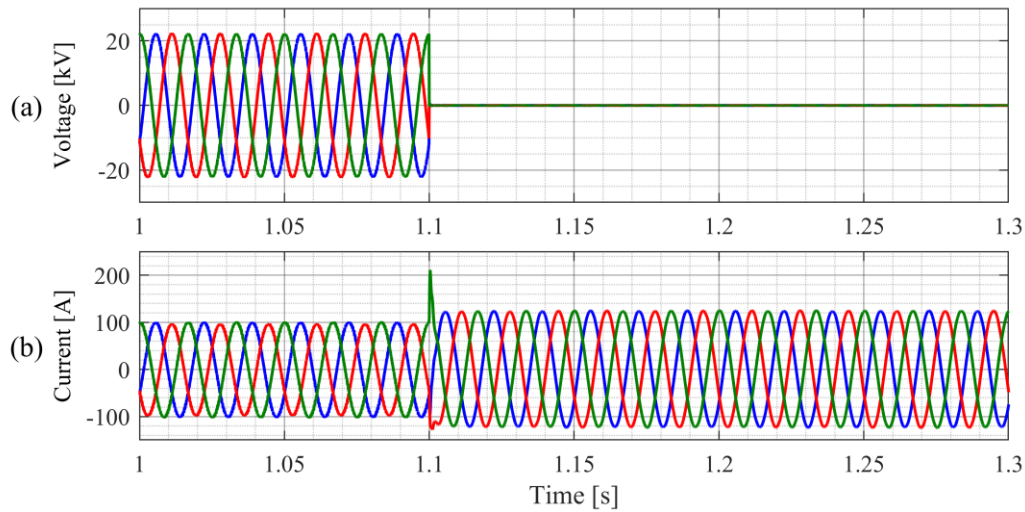
Figure 3.12. PV terminal voltage and current during a three-phase to ground fault.

The microgrid includes a PV generation system, a WT, two BESS, and highly unbalanced loads that are distributed along a 24 km main feeder. All DERs are inverter-interfaced. Detailed models of the DERs and their control strategies are reported in [65]. The microgrid is assumed to be low-reactance grounded and of the four-wire multi-grounded configuration [24]. The parameters and specifications of the study system components are given in the Appendix. Relay R1 in Fig. 3.11 is the IPR, and R2-R6 are MPRs.

The aforementioned study system is used to demonstrate the adverse effects of IIDERs on the operation of the NSDE and also to verify acceptable performance of the proposed protection strategy. For this purpose, different types of symmetrical and asymmetrical faults, including LG, LL, LLG, and three-phase faults have been applied to six different locations in the microgrid, shown as F1-F6 in Fig. 3.11. The fault resistance R_f is assumed to be zero, 10 Ω, and 50 Ω. The microgrid is in the steady-state before the faults are applied. The reported relay settings and simulation results are either in per-unit or the primary values, i.e., correspond to the values at the primary-sides of the instrument transformers.

Fig. 3.12 shows the output current of the PV plant during an internal three phase to ground fault in the grid-connected mode of operation. The plant operates at MPPT at maximum capacity before the faults at 1.05 s. It can be seen that the output of the converter is limited to 1.2 p.u. value for inverter protection.

3.3.1   NSDE in the Inverter-Dominated Microgrid

This part illustrates malfunction of the NSDE when its ECA is set at $\angle Z_{1L}$. Fig. 10 shows the negative-sequence impedances measured by relays R1-R6, under 99 asymmetrical fault instances with various fault types and fault resistances at locations F1-F6 shown in Fig. 3.11, under both grid-connected and islanded modes. To simplify the analysis, the measured impedances are divided into four categories in Fig. 3.13, depending on the grid-connection mode and the fault location with respect to the relay reference directions. Figs. 3.13 (c) and (d) show that the NSDE fails to detect the correct fault direction under a large portion of reverse faults, which confirms the theoretical analysis presented in Section 3.1.3 and illustrated in Fig. 3.7. Fig. 3.14 shows that the proposed solution, i.e., setting the ECA of the NSDE at zero degrees, effectively resolves the issue and provides maximum security margin for the relays. Fig. 3.14 also demonstrates the necessity of using an ECA of zero degrees, since any ECA below -15 degrees would cause issues under forward faults, Fig. 3.14(a), and any ECA above 10 degrees would cause issues under reverse faults, Fig. 3.14(c).
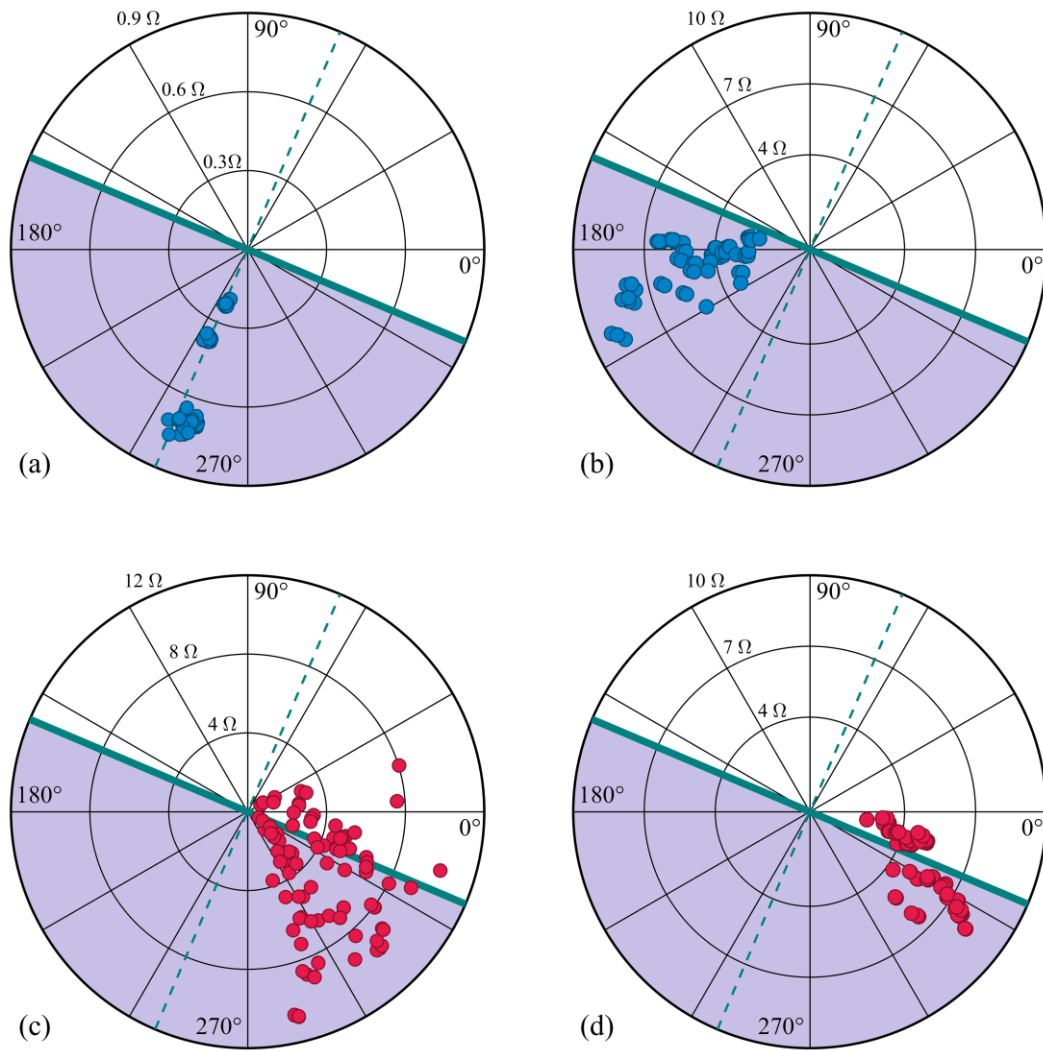
Figure 3.13 Negative-sequence impedances measured by relays R1-R6, under (a) forward faults in the grid-connected microgrid, (b) forward faults in the islanded microgrid, (c) reverse faults in the grid-connected microgrid, and (d) reverse faults in the islanded microgrid.
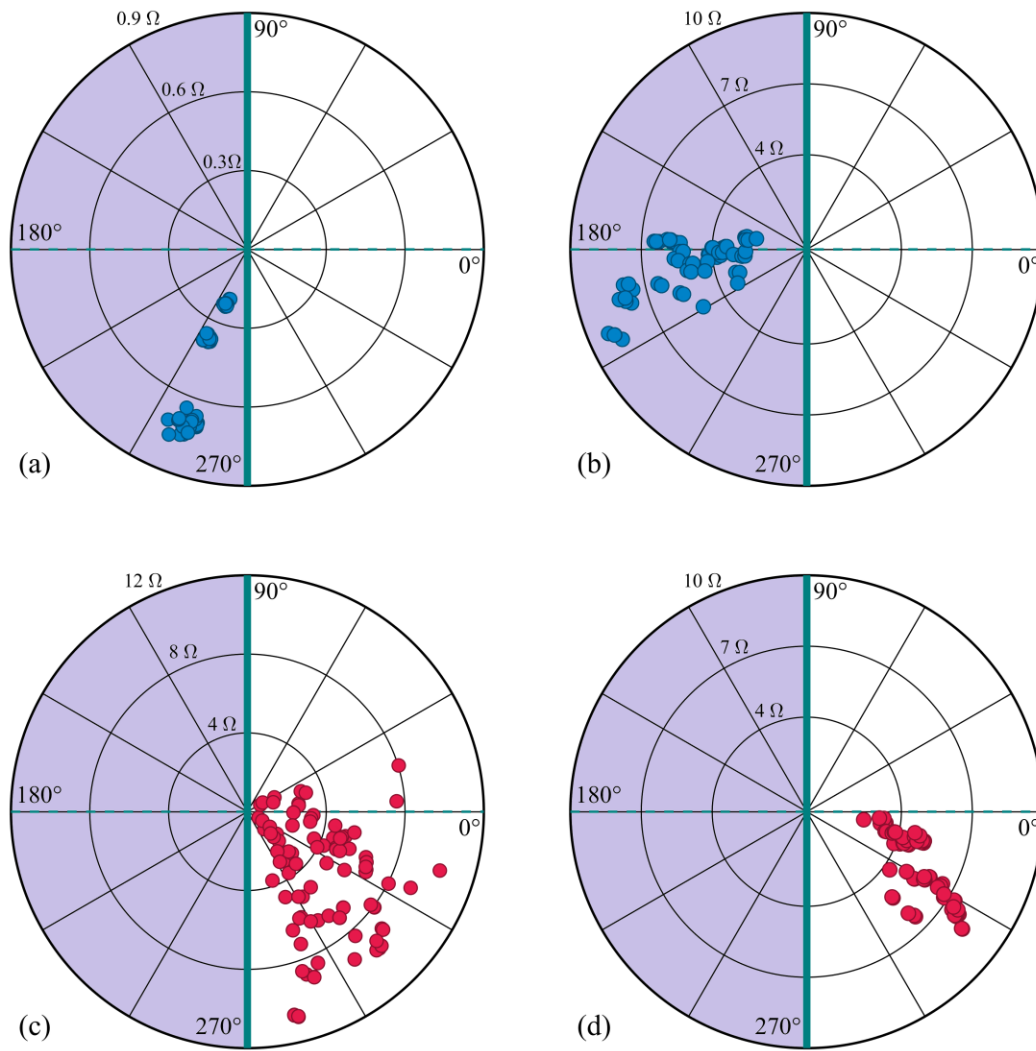
Figure 3.14 Negative-sequence impedances measured by relays R1-R6, under (a) forward faults in the grid-connected microgrid, (b) forward faults in the islanded microgrid, (c) reverse faults in the grid-connected microgrid, and (d) reverse faults in the islanded microgrid.

3.3.2 Performance of the Proposed Protection Strategy

This part evaluates the performance of the proposed non-pilot protection strategy in protecting the study system of Fig. 3.11. The relays R1-R6 are coordinated with each other and with the downstream fuses according to the coordination strategy introduced in part 3.2.3. Coordination of the forward and reverse elements of the relays is performed separately, as follows:

TABLE I
RELAY TYPES AND SETTINGS

Relay	Type	TD_{fwd} (ms)	TD_{rev} (ms)	Pick Up Settings			
				$I_{P\text{-}PU}$ (A)	$V_{P\text{-}PU}$ (p.u.)	$I_{2\text{-}PU}$ (A)	$V_{2\text{-}PU}$ (p.u.)
R1	IPR	200	50	800	0.5	32	0.1
R2	MPR	800	250	-	0.5	28	0.1
R3	MPR	600	450	-	0.5	16	0.1
R4	MPR	650	-	-	0.5	16	0.1
R5	MPR	400	850	-	0.5	8	0.1
R6	MPR	400	-	-	0.5	8	0.1

Forward-directional elements: $R_2 \rightarrow R_3 \rightarrow (R_5 \text{ and } R_6) \rightarrow R_1$

Reverse-directional elements: $R_5 \rightarrow R_4 \rightarrow R_3 \rightarrow R_2 \rightarrow R_1$

The notation $R_j \rightarrow R_k$ means that, for faults downstream of both relays R_j and R_k, either in their forward or reverse direction, R_j operates with a larger delay as compared with R_k. It should be noted that R1 operates faster than all relays in both directions, because it is the IPR and must trip before all MPRs under all fault conditions. In addition, R6 does not include a reverse directional elements, because it is installed on a passive feeder that would never feed reverse faults. R4 also does not include a reverse directional element due to the presence of R6 and R4 on the same bus. A reverse element in R4 would be redundant and would increase the forward operating times of R3 and R2 by 200 ms. The relay settings are shown in Table I.

Faults of different types with various resistances are applied to different locations under both grid-connected and islanded operating modes of the microgrid. Tables II and III show the operating time delays of the relays and the TCTs of the fuses that protect the faulted laterals (if applicable), for internal faults. Table IV shows the relay operating time delays under external faults. The study results show that the proposed protection strategy selectively and reliably protects the microgrid under both operation modes under all fault conditions.

TABLE II

RELAY AND FUSE OPERATING TIME DELAYS IN GRID-CONNECTED MODE

Fault			Operating time (ms)						
Location	Type	R_f	R1	R2	R3	R4	R5	R6	Fuse
F1	AG	0	205	256	455	656	856	-	-
		10	206	263	459	663	893	-	-
		50	207	555	755	955	1169	-	-
	AB	0	203	253	453	653	853	-	-
		10	203	254	453	655	855	-	-
		50	204	554	755	955	1171	-	-
	ABG	0	202	253	453	654	853	-	-
		10	202	264	486	688	884	-	-
		50	212	596	785	985	1205	-	-
	ABC	0	234	269	459	662	862	-	-
F2	AG	0	206	805	455	656	873	-	22
		10	206	806	456	657	890	-	35
		50	208	826	500	718	1170	-	153
	AB	0	203	803	453	653	853	-	16
		10	203	803	453	654	853	-	23
		50	204	832	497	698	899	-	75
	ABG	0	202	822	453	654	853	-	15
		10	203	822	460	662	860	-	27
		50	212	940	782	985	1205	-	142
	ABC	0	207	815	469	659	859	-	14
F3	AG	0	206	806	606	655	872	-	33
		10	206	806	606	656	875	-	47
		50	208	847	628	683	896	-	172
	AB	0	204	804	603	653	853	-	26
		10	204	804	603	654	853	-	33
		50	205	805	604	660	876	-	88
	ABG	0	203	803	602	654	854	-	24
		10	204	838	602	655	856	-	36
		50	213	922	634	988	1198	-	151
	ABC	0	212	1106	897	663	863	-	22
F4	AG	0	207	806	606	-	402	-	45
		10	207	824	606	-	405	-	61
		50	208	847	628	-	423	-	194
	AB	0	204	804	603	-	403	-	36
		10	204	804	603	-	403	-	44
		50	205	805	604	-	403	-	103
	ABG	0	204	804	603	-	402	-	32
		10	204	821	603	-	402	-	44
		50	213	918	634	-	434	-	167
	ABC	0	216	1113	907	-	415	-	29
F5	AG	0	206	806	606	-	872	405	32
		10	206	806	606	-	875	405	47
		50	208	846	628	-	896	424	181
	AB	0	204	804	603	-	853	402	26
		10	204	804	603	-	853	402	34
		50	205	805	604	-	876	402	90
	ABG	0	203	823	620	-	854	420	24
		10	204	838	602	-	856	401	36
		50	213	922	634	-	1198	433	158
	ABC	0	212	1107	897	-	863	413	22

TABLE III

RELAY AND FUSE OPERATING TIME DELAYS IN ISLANDED MODE

Fault			Operating time (ms)					
Location	Type	R_f	R2	R3	R4	R5	R6	Fuse
F1	AG	0	253	452	653	852	-	-
		10	258	453	654	853	-	-
		50	260	458	659	859	-	-
	AB	0	256	452	655	856	-	-
		10	256	456	656	856	-	-
		50	257	456	657	857	-	-
	ABG	0	257	457	657	857	-	-
		10	258	457	658	858	-	-
		50	266	465	665	866	-	-
	ABC	0	259	459	659	859	-	-
F2	AG	0	803	452	653	852	-	76
		10	808	452	654	853	-	97
		50	812	458	659	859	-	256
	AB	0	807	452	655	856	-	210
		10	807	455	656	856	-	239
		50	809	456	657	857	-	252
	ABG	0	815	457	657	857	-	102
		10	815	457	658	858	-	139
		50	822	465	665	865	-	268
	ABC	0	809	459	659	859	-	207
F3	AG	0	803	603	653	852	-	81
		10	808	604	654	853	-	101
		50	812	610	658	859	-	263
	AB	0	807	606	655	856	-	212
		10	808	606	656	856	-	244
		50	809	607	657	857	-	257
	ABG	0	815	607	657	857	-	106
		10	815	607	658	857	-	142
		50	822	615	665	865	-	262
	ABC	0	809	609	659	859	-	195
F4	AG	0	0	804	604	-	403	-
		10	10	808	608	-	403	-
		50	50	812	610	-	404	-
	AB	0	0	808	606	-	406	-
		10	10	808	606	-	406	-
		50	50	810	607	-	406	-
	ABG	0	0	815	607	-	406	-
		10	10	816	608	-	407	-
		50	50	822	615	-	408	-
	ABC	0	0	813	613	-	412	-
F5	AG	0	0	803	603	-	852	402
		10	10	808	604	-	853	402
		50	50	812	610	-	859	402
	AB	0	0	807	606	-	856	402
		10	10	808	606	-	856	405
		50	50	809	607	-	857	406
	ABG	0	0	815	607	-	857	402
		10	10	815	607	-	857	402
		50	50	822	615	-	865	406
	ABC	0	0	809	609	-	859	409

TABLE IV

RELAY OPERATING TIME DELAYS FOR THE EXTERNAL FAULT

Fault			Operating time (ms)				
Location	Type	R_f	R1	R2	R3	R4	R5
F6	AG	0	56	257	456	657	888
		10	64	267	463	666	896
		50	154	364	564	763	977
	AB	0	53	253	453	653	853
		10	54	256	456	660	875
		50	152	354	554	754	966
	ABG	0	53	253	453	653	853
		10	60	364	522	739	936
		50	176	397	577	797	994
	ABC	0	259	459	659	859	-

For the cases where the fault is applied to a lateral circuit protected by a fuse, i.e. F2-F5, the corresponding lateral fuse is the first protective device that operates, as shown in Tables II and III. Table III also shows that the reduced fault current level in the islanded microgrid increases the fuse TCTs. However, in both grid-connected and islanded modes, the minimum margin of about 200 ms is maintained between the operation times of all protective devices that see the fault in the same direction.

The maximum operating time of all protective devices under the investigated fault conditions is about 1205 ms. The results of the comprehensive studies conducted in this study indicate that this delay does not result in instability of the inverter-dominated microgrid. Besides, it should be noted that the aforementioned delay is due to the fact that six relays and a fuse are coordinated in the utilized study system. In most cases, a smaller number of relays would be needed in each microgrid feeder, which would reduce the maximum relay operation time.

3.4   Conclusions

A fast, selective, and reliable non-pilot protection strategy is proposed for the inverter-dominated microgrid. A simple and effective method is also introduced for appropriate setting and application of the NSDE for reliable determination of asymmetrical fault direction in the inverter-dominated microgrid. The study results indicate that the proposed protection strategy (i) is applicable to both grid-connected and islanded microgrids, (ii) enables operation of lateral fuses, (iii) prevents microgrid exposure to prolonged fault currents from the utility grid, (iv) minimizes microgrid exposure to voltage sags during utility grid faults, and (v) can be implemented using the existing commercial relays.

Chapter 4

4 Hardware Implementation

The proposed protection strategy is tested using an off-the-shelf commercial relay. The proposed strategy is implemented in a SEL-351 relay and evaluated using the SEL-AMS industrial relay testing platform. The investigation verifies that the proposed microgrid protection strategy performs as expected for fast and reliable detection of faults in the inverter-dominated microgrid and can be implemented in the commercially available relays.

4.1 Relay Setting

The relay logic and settings are set based on the proposed protection strategy introduced in Section 3.2 using the AcSELerator® QuickSet software. Fig. 4.1 shows the graphical representation of the protection algorithm implemented in the SEL-351 relay shown in the AcSELerator software provided by the relay manufacturer. Other relay settings such as pickup voltage, pickup current and the time delay for the trip signal are set through the settings editor panel shown in Fig. 4.2.

Figure 4.1 Graphical logic representation of the MPR algorithm using AcSELerator® QuickSet software.

Settings Editor - New Settings 4 (SEL-351-7 106 v6.4.0.2)

▲ ● Global
    ○ General
    ○ Optoisolated Input Timers
    ○ Breaker Monitor
    ○ Synchronized Phasor Measurement Settings
    ○ DNP Settings
    ○ Time And Date Management Settings
▲ ● Group 1
  ▲ ● Set 1
    ○ General Settings
    ○ Line Settings and Fault Locator
    ○ Phase Overcurrent Elements
    ○ Neutral Ground Overcurrent Elements
    ○ Residual Ground Overcurrent Elements
    ○ Negative-Sequence Overcurrent Elements
    ○ Phase Time-Overcurrent Elements
    ○ Neutral Ground Time-Overcurrent Element
    ○ Residual Ground Time-Overcurrent Elements
    ○ Negative-Sequence Time-Overcurrent Element
    ○ Breaker Failure
    ○ Second Harmonic Blocking
    ○ Load Encroachment Element
    ○ Directional Elements
    ● Voltage Elements
    ○ Synchronism Check Elements
    ○ Frequency Elements
    ○ Rate-of-Change-of-Frequency Elements
    ○ Reclosing Relay
    ○ Switch-Onto-Fault Logic
    ○ Communications Assisted Trip Schemes
    ○ Demand Elements
    ○ Other Settings
    ○ SELogic Variable Timers
    ○ Power Elements
    ○ Voltage Sag/Swell/Interrupt Elements
  ▲ ● Logic 1
    ○ Trip/Communication-Assisted Trip Logic
    ○ Close/Reclose Logic
    ○ Latch Bits Set/Reset
    ○ Torque Control
    ○ Breaker Failure Equations
    ○ Logic Variable Equations
    ○ SELogic Variable Timer Inputs
    ○ Output Contacts
    ○ Display Points
    ○ Setting Group Selection
    ○ Other Equations
    ○ Mirrored Bits Transmit Equations
    ○ Reset Equations
    ○ PMU Trigger Equations
  ○ Graphical Logic 1

Voltage Elements

Voltage Element Settings

EVOLT Voltage Elements

Y   ▼   Select: Y, N

Phase Undervoltage Elements

27P1P Phase Undervoltage Pickup (V,sec)

57.50   Range = 0.00 to 300.00, OFF

27P2P Phase Undervoltage Pickup (V,sec)

OFF   Range = 0.00 to 300.00, OFF

Phase Overvoltage Elements

59P1P Phase Overvoltage Pickup (V,sec)

OFF   Range = 0.00 to 300.00, OFF

59P2P Phase Overvoltage Pickup (V,sec)

OFF   Range = 0.00 to 300.00, OFF

Sequence Overvoltage Elements

59N1P Zero-Seq (3V0) Overvolt. PU (V,sec)

OFF   Range = 0.00 to 300.00, OFF

59N2P Zero-Seq (3V0) Overvolt. PU (V,sec)

OFF   Range = 0.00 to 300.00, OFF

59QP Neg-Seq (V2) Overvoltage PU (V,sec)

11.50   Range = 0.00 to 200.00, OFF

59Q2P Neg-Seq (V2) Overvoltage PU (V,sec)

OFF   Range = 0.00 to 120.00, OFF

59V1P Pos-Seq (V1) Overvoltage PU (V,sec)

OFF   Range = 0.00 to 300.00, OFF

Channel VS Voltage Elements

27SP Channel VS Undervoltage PU (V,sec)

OFF   Range = 0.00 to 300.00, OFF

59S1P Channel VS Overvoltage PU (V,sec)

OFF   Range = 0.00 to 300.00, OFF

59S2P Channel VS Overvoltage PU (V,sec)

OFF   Range = 0.00 to 300.00, OFF

Part#: 035172C3E54XX2   Group 1 : Voltage Elements   351_settings_PlayBack.rdb

Figure 4.2 Settings editor window of AcSELerator® QuickSet software.

Figure 4.3 Hardware setup for testing relay R5 during a solid phase-to-ground forward fault.

Figure 4.4 Front panel screen of SEL-351 detecting the forward asymmetrical fault.

4.2   Relay Testing Results

To verify the performance of the proposed protection strategy, voltage and current measurements at the relay locations shown in Fig. 3.11 for different fault conditions are downloaded from the PSCAD simulation and then played back to SEL-351 using SEL SEL-AMS relay testing platform. Fig. 4.3 shows testing of relay R5 for a solid phase-to-ground fault at fault location F4.3 and 4. Similarly, relay R2 is tested during a 10 Ω three-phase fault at location F1 as shown in Fig. 4.5 and 6.
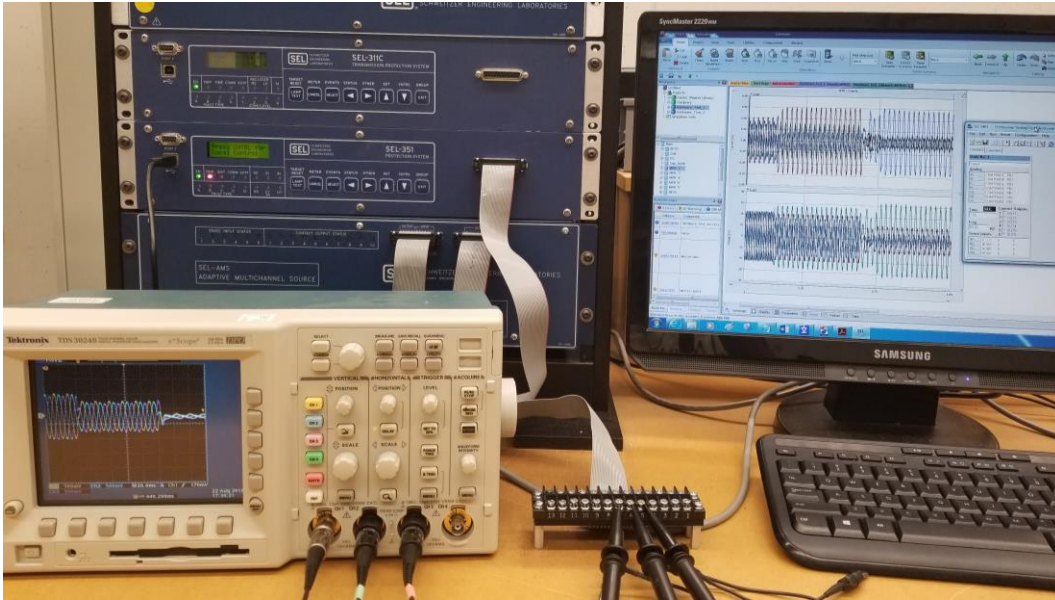
Figure 4.5 Hardware setup for testing relay R2 during a 10 Ω three-phase reverse fault.

Figure 4.6 Front panel screen of SEL-351 detecting the reverse symmetrical fault.

It can be seen that the relays successfully detect the fault type and direction. The operation time for each relay is verified by exporting each fault event from SEL-351. Fig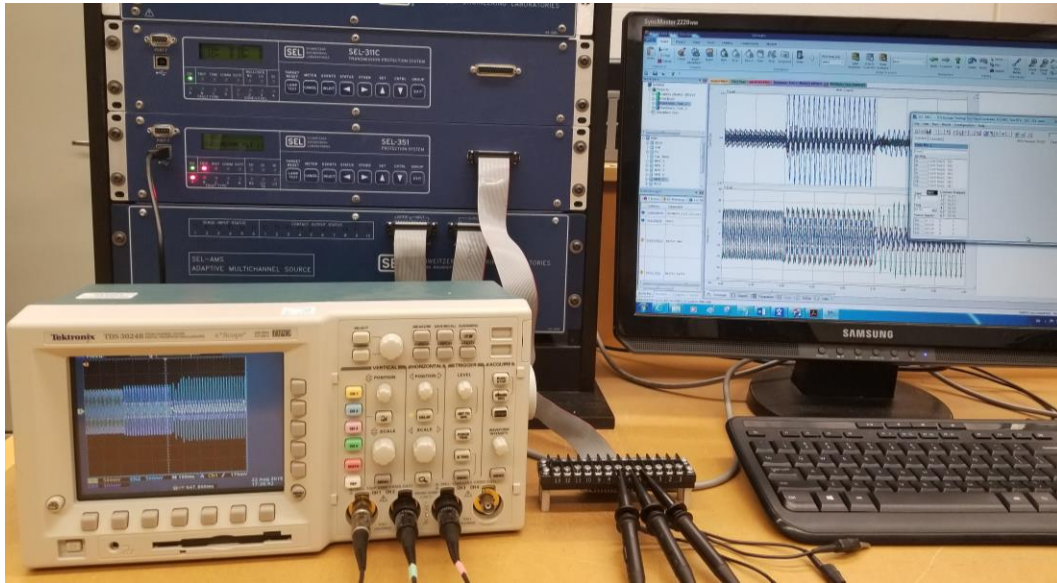. 4.7 shows the saved fault event by relay R5 after a forward phase-to-ground fault. It can be seen that the trip signal is triggered 400 ms after the fault inception, which is the exact amount the relay was coordinated for. Similarly, Fig. 4.8 shows that relay R2 trips 250 ms after the inception of the reverse fault, as planned.
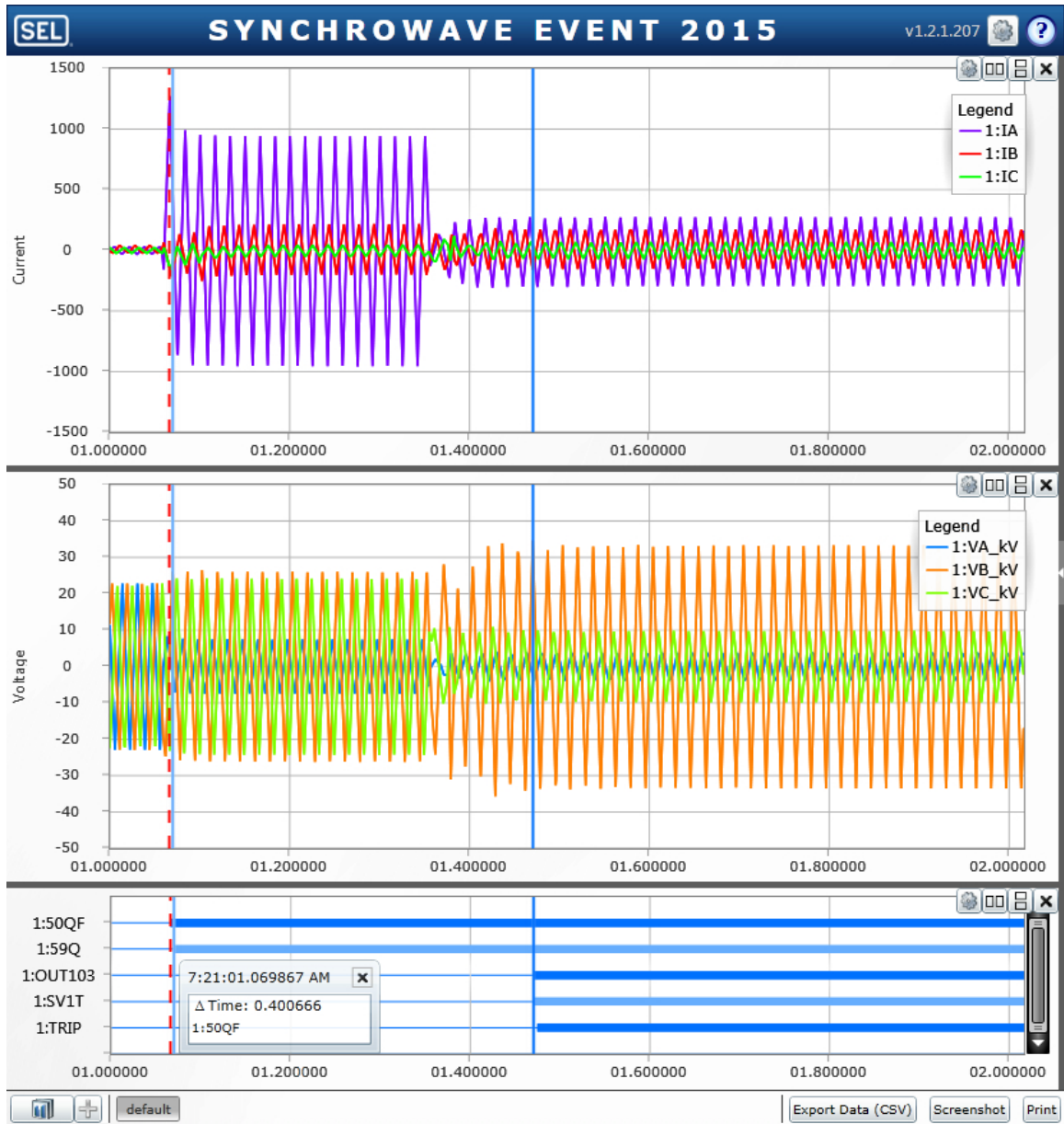
Figure 4.7 The event file saved by relay R5 implementation during a solid phase-to-ground fault at location F4 i.e., forward fault.
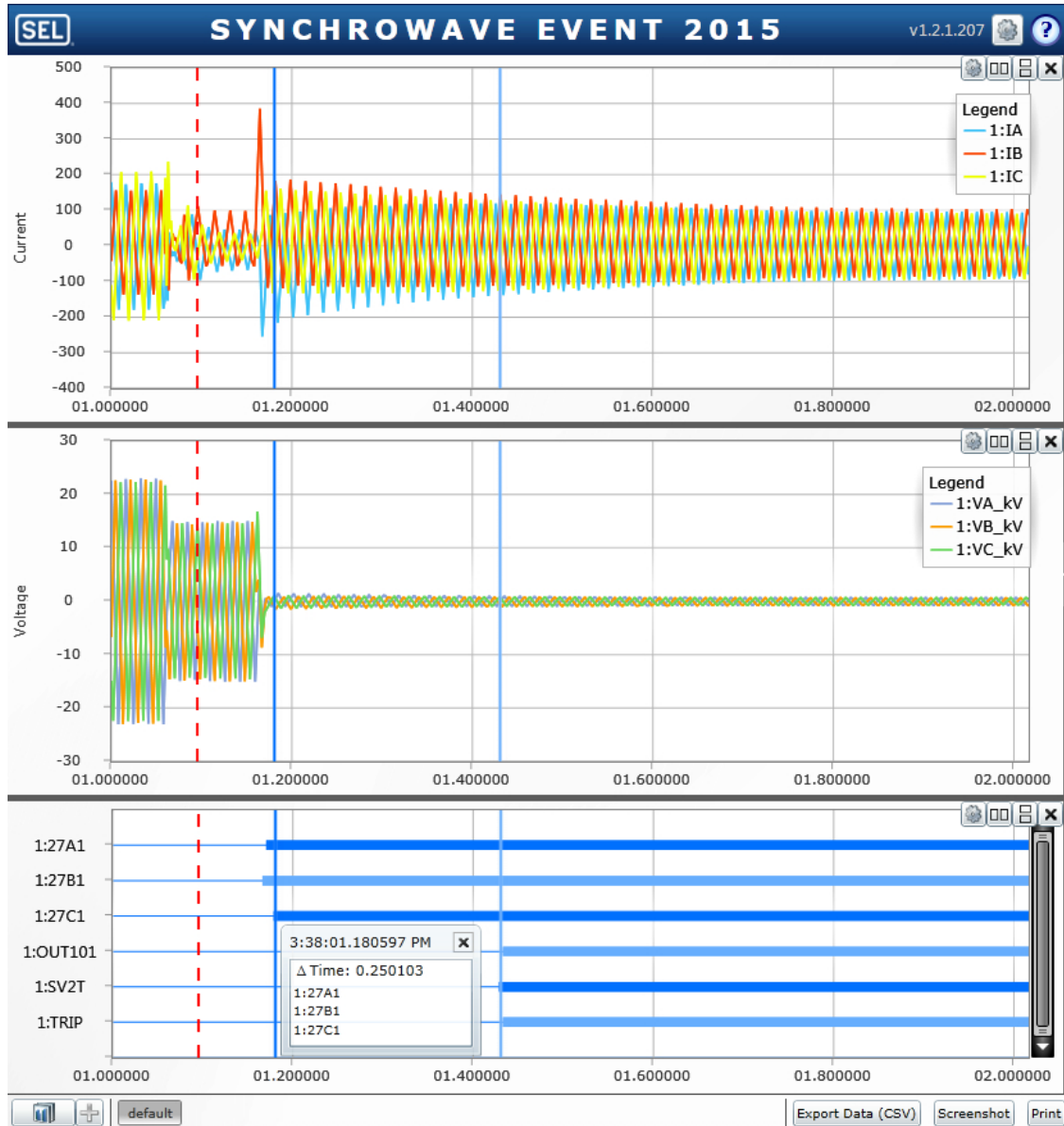
Figure 4.8 The event file saved by relay R2 implementation during a 10 Ω three-phase fault at location F1.

4.3   Conclusions

This chapter presented the results of the hardware implementation of the proposed protection strategy in a commercially available relay. It was shown that the protection strategy can be implemented on the existing hardware. The relays operated reliably and coordinately under different fault conditions in both modes of microgrid operation without any communication or adaptive requirements.

Chapter 5

5   Summary and Conclusions

The microgrid technology offers significant advantages, however, the lack of a cost-effective, selective, and reliable strategy to protect the AC microgrid has constrained the proliferation of this highly advantageous technology. Protection system design and verification cannot be performed without an effective control strategy that maintains microgrid stability and provides acceptable dynamics response to disturbances and faults.

The main objectives of this research are to develop a selective and reliable non-pilot protection strategy and the associated relay technologies for the inverter-dominated microgrid and to identify the most suitable control strategy and making improvements necessary for stable operation of the inverter-dominated.

An improved PD droop control strategy for effective power sharing and frequency/voltage regulation is proposed that damps power oscillations between DERs, limits frequency deviations, and improves the stability and disturbance response in the islanded inverter-dominated AC microgrid.

The proposed protection strategy (i) utilizes improved symmetrical components-based, i.e., sequence-domain, directional elements for increased reliability, (ii) does not require communication signals or adaptive settings, (iii) is not adversely affected by the limited fault current contributions of IIDERs, (iv) is robust against variations of the fault current magnitude (v) enables coordination of relays with fuses protecting the laterals and non-critical circuits, and (vi) operates reliably and selectively in inverter-dominated microgrids with significant load unbalance (v) can be implemented using the existing commercial relays. Acceptable performance of the proposed protection strategy is verified using numerous fault studies conducted on a realistic study system in the PSCAD/EMTDC software environment, and hardware implementation.

Appendix A: Sandia Frequency-Shift Active Islanding Detection

The inverter phase angle ϕ_{inv} can be expressed as the following [40], [41]:

$$\phi_{inv} = \pi k (f - f_n)/2$$

where f is the island frequency, f_n the nominal frequency, and k is the SFS parameter. This detection method can be implemented in DER output controller by shifting the reference values in the current loop of the converter. Fig. A.1 shows the inner loop of an IIDER with SFS module.
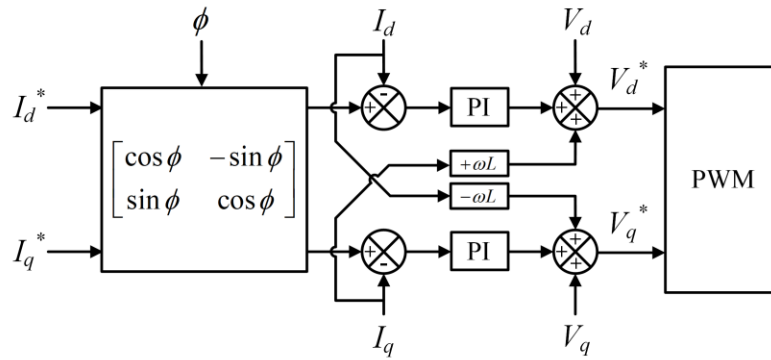
Figure A.1. IIDER interface control with SFS active islanding detection.

Appendix B: Study System Parameters

TABLE B.I
STUDY SYSTEM PARAMETERS

Component	Description
Grid	$V_{LL\text{-}base}$ = 27.6 kV, 60 Hz S_{nom} = 20 MVA, SSC = 885.33, X/R = 10
Wind power plant	S_{WPP} = 4 MVA = 2×2 MVA
PV power plant	S_{PV} = 3.5 MVA
BESS units	S_{BESS} = 2×2 MVA
Capacitor bank	Q = 1.5 MVAR

Transformers	T1: 3.6 MVA, 6% impedance
	    27.6 kV/8.31 kV, ΔY
	T2: 15 MVA, 7.3% impedance
	    27.6 kV/27.6 kV, YY
	T3: 1 MVA, 4% impedance
	    27.6 kV/8.31 kV, ΔY
	T4: 3.6 MVA, 5.65% impedance
	    27.6 kV/8.31 kV, ΔY

Overhead lines	Spacing ID = STD-3PH-NBP [66] R_1 = 0.172 Ω/km, R_0 = 0.491 Ω/km X_1 = 0.404 Ω/km, X_0 = 1.354 Ω/km B_1 = 4.171 uS/km, B_0 = 1.759 uS/km
Fuse	20A-E, BA2 Type Expulsion Fuse [67]

TABLE B.II
OVERHEAD LINE LENGTH

Line	Length (m)	Line	Length (m)	Line	Length (m)
L1	5700	L11	3330	L21	1550
L2	1010	L12	1030	L22	2120
L3	400	L13	3490	L23	1820
L4	380	L14	1430	L24	2540
L5	120	L15	190	L25	620
L6	170	L16	1940	L26	3580
L7	260	L17	2450	L27	770
L8	140	L18	1630	L28	2080
L9	940	L19	1200	L29	4510
L10	300	L20	820	L30	4040

TABLE III

BALANCED /LOAD SPECIFICATIONS

Load Name	Three Phase (kVA)	Power Factor
1	2364	0.95
2	346	0.87
3	3355	0.95
4	256	0.75
5	6.3	1
6	265	0.95
7	650	1
8	50	0.95
9	160	0.95
10	205	1
11	445	0.95
12	10	0.95
13	215	0.95
14	85	0.95
15	110	0.95
16	2280	0.95

TABLE IV

UNBALANCED /LOAD SPECIFICATIONS

Load Name	Phase A (kVA)	Phase B (kVA)	Phase C (kVA)	Power Factor
1	731.22	741.22	891.22	0.95
2	115.33	115.33	115.33	0.87
3	1099.00	946.00	1310.00	0.95
4	85.33	85.33	85.33	0.75
5	2.10	2.10	2.10	1
6	186.67	41.67	36.67	0.95
7	216.67	216.67	216.67	1
8	0.00	50.00	0.00	0.95
9	160.00	0.00	0.00	0.95
10	0.00	0.00	205.00	1
11	146.67	126.67	171.67	0.95
12	10.00	0.00	0.00	0.95
13	0.00	0.00	215.00	0.95
14	0.00	85.00	0.00	0.95
15	60.00	0.00	50.00	0.95
16	749.00	710.00	821.00	0.95

TABLE V

DROOP CHARACTERISTICS

Strategy	Frequency Droop	Voltage Droop
Conventional Droop	$\omega = \omega^* - 0.008 \times P$	$V = V^* - 0.1 \times Q$
PD Droop	$\omega = \omega^* - (0.008 + \dfrac{0.05 \times s}{s+2}) \times P$	$V = V^* - 0.1 \times Q$
Improved PD Droop with P damping	$\omega = \omega^* - (0.008 + \dfrac{0.05 \times s}{s+100}) \times P$	$V = V^* - 0.1 \times Q$
Improved PD Droop with P and Q damping	$\omega = \omega^* - (0.008 + \dfrac{0.05 \times s}{s+100}) \times P$	$V = V^* - (0.1 + \dfrac{0.1 \times s}{s+50}) \times Q$

References

[1]   S. Parhizi, H. Lotfi, A. Khodaei and S. Bahramirad, "State of the Art in Research on Microgrids: A Review," in *IEEE Access*, vol. 3, pp. 890-925, 2015.

[2]   Department of Energy Office of Electricity Delivery and Energy Reliability. (2012). Summary Report: 2012 DOE Microgrid Workshop.

[3]   M. A. Zamani, "Protection and control of active distribution networks and microgrids," Ph.D. dissertation, Dept. Elect. Comp. Eng., Western Univ., London, ON, Canada, 2012. Electronic Thesis and Dissertation Repository. 1046. http://ir.lib.uwo.ca/etd/1046

[4]   K. T. Tan, P. L. So, Y. C. Chu, and M. Z. Q. Chen,"Coordinated Control and Energy Management of Distributed Generation Inverters in a Microgrid", in *IEEE Transaction on Power Delivery*, vol. 28, no. 2, pp. 704–713, Apr. 2013.

[5]   J. Rocabert, A. Luna, F. Blaabjerg and P. Rodríguez, "Control of Power Converters in AC Microgrids," in *IEEE Transaction on Power Electronics*, vol. 27, no. 11, pp. 4734-4749, Nov. 2012.

[6]   A. Hooshyar and R. Iravani, "Microgrid Protection," *in Proceedings of the IEEE*, vol. 105, no. 7, pp. 1332-1353, July 2017.

[7]   A. A. Memon, K. Kauhaniemi, "A critical review of AC microgrid protection issues and available solutions," *Electric Power Systems Research*, vol. 129, pp. 23-31, 2015.

[8]   Z. Chen, X. Pei, M. Yang, L. Peng, P. Shi, "A Novel Protection Scheme for Inverter-Interfaced Microgrid (IIM) Operated in Islanded Mode," *IEEE Trans. Power Electron.*, vol. 33, no. 9, pp. 7684-7697, Sept. 2018.

[9]   H. M. Sharaf, H. H. Zeineldin and E. El-Saadany, "Protection coordination for microgrids with grid-connected and islanded capabilities using communication assisted dual setting directional overcurrent relays," *IEEE Trans. Smart Grid*, vol. 9, no. 1, pp. 143-151, Jan. 2018.

[10]   S. Mirsaeidi, D. M. Said, M. W. Mustafa, M. H. Habibuddin, K. Ghaffari, "An analytical literature review of the available techniques for the protection of micro-grids," *International Journal of Electrical Power & Energy Systems*, vol. 58, pp. 300-306, 2014.

[11]   S. F. Zarei and M. Parniani, "A comprehensive digital protection scheme for low-voltage microgrids with inverter-based and conventional distributed generations," *IEEE Trans. Power Del.*, vol. 32, no. 1, pp. 441-452, Feb. 2017.

[12]   M. A. Zamani, A. Yazdani and T. S. Sidhu, "A communication-assisted protection strategy for inverter-based medium-voltage microgrids," *IEEE Trans. Smart Grid*, vol. 3, no. 4, pp. 2088-2099, Dec. 2012.

[13]   W. Guo, L. Mu and X. Zhang, "Fault models of inverter-interfaced distributed generators within a low-voltage microgrid," *IEEE Trans. Power Del.*, vol. 32, no. 1, pp. 453-461, Feb. 2017.

[14]   Z. Shuai, C. Shen, X.Yin, X.Liu and Z.J.Shen, "Fault Analysis of Inverter-Interfaced Distributed Generators With Different Control Schemes," *IEEE Trans. Power Del.,* vol. 33, no. 3, pp. 1223-1235, June 2018.

[15]   E. Sortomme, S. S. Venkata and J. Mitra, "microgrid protection using communication-assisted digital relays," *IEEE Trans. Power Del.*, vol. 25, no. 4, pp. 2789-2796, Oct. 2010.

[16]   H. F. Habib, C. R. Lashway and O. A. Mohammed, "A review of communication failure impacts on adaptive microgrid protection schemes and the use of energy storage as a contingency," *IEEE Trans. Ind. Appl.*, vol. 54, no. 2, pp. 1194-1207, Mar.-Apr. 2018.

[17]   H. Muda and P. Jena, "Superimposed adaptive sequence current based microgrid protection: a new technique," *IEEE Trans. Power Del.*, vol. 32, no. 2, pp. 757-767, Apr. 2017.

[18]   H. Laaksonen, D. Ishchenko and A. Oudalov, "Adaptive protection and microgrid control design for Hailuoto island," *IEEE Trans. Smart Grid*, vol. 5, no. 3, pp. 1486-1493, May 2014.

[19]   P. Mahat, Z. Chen, B. Bak-Jensen, C. Bak, "A simple adaptive overcurrent protection of distribution systems with distributed generation," *IEEE Trans. Smart Grid*, vol. 2, no. 3, pp. 428-437, Sept. 2011.

[20]   H. Al-Nasseri, M. A. Redfern and F. Li, "A voltage based protection for micro-grids containing power electronic converters," *IEEE PES General Meeting*, Montreal, QC, 2006.

[21]   D. P. Mishra, S. R. Samantaray and G. Joos, "A Combined Wavelet and Data-Mining Based Intelligent Protection Scheme for Microgrid," *IEEE Trans. Smart Grid*, vol. 7, no. 5, pp. 2295-2304, Sept. 2016.

[22]   H. Nikkhajoei and R. H. Lasseter, "Microgrid Protection," 2007 *IEEE Power Engineering Society General Meeting*, Tampa, FL, 2007, pp. 1-6.

[23]   M. A. Zamani, T. S. Sidhu and A. Yazdani, "A protection strategy and microprocessor-based relay for low-voltage microgrids," *IEEE Trans. Power Del.,* vol. 26, no. 3, pp. 1873-1883, Jul. 2011.

[24]   J. Mohammadi, F. B. Ajaei and G. Stevens, "Grounding the AC microgrid," *IEEE Trans. Ind. Appl.*, vol. PP, no. P, pp. 1-8, Jul. 2018.

[25]   D. E. Olivares et al., "Trends in Microgrid Control," *IEEE Transactions on Smart Grid*, vol. 5, no. 4, pp. 1905-1919, July 2014.

[26]   A. Yazdani et al., "Modeling Guidelines and a Benchmark for Power System Simulation Studies of Three-Phase Single-Stage Photovoltaic Systems," *IEEE Trans. Power Del.*, vol. 26, no. 2, pp. 1247-1264, April 2011.

[27] J. M. Guerrero, P. C. Loh, T. L. Lee and M. Chandorkar, "Advanced Control Architectures for Intelligent Microgrids—Part II: Power Quality, Energy Storage, and AC/DC Microgrids," *IEEE Trans. Ind. Electron.*, vol. 60, no. 4, pp. 1263-1270, April 2013.

[28] H. Han, X. Hou, J. Yang, J. Wu, M. Su and J. M. Guerrero, "Review of Power Sharing Control Strategies for Islanding Operation of AC Microgrids," *IEEE Trans. Smart Grid*, vol. 7, no. 1, pp. 200-215, Jan. 2016.

[29] T. L. Vandoorn, J. D. M. De Kooning, B. Meersman, and L. Vandevelde, "Review of primary control strategies for islanded microgrids with power-electronic interfaces," *Elsevier, Renewable and Sustainable Energy Reviews*, vol. 19, pp. 613–628, 2013.

[30] D. Shanxu, M. Yu, and X. Jian, "Parallel operation control technique of voltage source inverters in UPS," *Proc. of the IEEE 1999 International Conf.* 1999, pp. 883-887.

[31] Y. Pei, G. Jiang, and X. Yang, "Auto-master-slave control technique of parallel inverters in distributed AC power systems and UPS," *Proc. 35th Annual IEEE Power Electron. Specialists*, 2004, pp. 2050-2053.

[32] A. M. Roslan, K. H. Ahmed, S. J. Finney and B. W. Williams, "Improved Instantaneous Average Current-Sharing Control Scheme for Parallel-Connected Inverter Considering Line Impedance Impact in Microgrid Networks," *IEEE Trans. Power Electron.*, vol. 26, no. 3, pp. 702-716, Mar. 2011.

[33] C. L. Chen, Y. Wang, J. S. Lai, Y. S. Lee and D. Martin, "Design of Parallel Inverters for Smooth Mode Transfer Microgrid Applications," *IEEE Trans. Power Electron.*, vol. 25, no. 1, pp. 6-15, Jan. 2010.

[34] Tsai-Fu Wu, Yu-Kai Chen and Yong-Heh Huang, "3C strategy for inverters in parallel operation achieving an equal current distribution," *IEEE Trans. Ind. Electron.*, vol. 47, no. 2, pp. 273-281, Apr. 2000.

[35] M. Prodanovic and T. C. Green, "High-Quality Power Generation Through Distributed Control of a Power Park Microgrid," *IEEE Trans. Ind. Elect.*, vol. 53, no. 5, pp. 1471-1482, Oct. 2006.

[36] P. H. Divshali, A. Alimardani, and S. H. Hosseinian, "Decentralized cooperative control strategy of DERs for stabilizing autonomous VSC-based microgrids," *IEEE Trans. Power Syst.*, vol. 24, no. 4, pp. 1949-1959, Nov. 2012.

[37] U. B. Tayab, M. A. B. Roslan, L. J. Hwai, and M. Kashif "A review of droop control techniques for microgrid," *Elsevier, Renewable and Sustainable Energy Reviews*, vol. 76, pp. 717-727, 2017.

[38] Y. Sun, X. Hou, J. Yang, H. Han, M. Su and J. M. Guerrero, "New Perspectives on Droop Control in AC Microgrid," *IEEE Trans. Ind. Electronics*, vol. 64, no. 7, pp. 5741-5745, July 2017.

[39] A.Yazdani, R. Iravani, Voltage-Sourced Converters in Power Systems. Hoboken, NJ: John Wiley & Sons, Inc., 2010.

[40] H. H. Zeineldin and S. Kennedy, "Sandia Frequency-Shift Parameter Selection to Eliminate Nondetection Zones," *IEEE Trans. Power Del.*, vol. 24, no. 1, pp. 486-487, Jan. 2009.

[41] H. H. Zeineldin and S. Conti, "Sandia frequency shift parameter selection for multi-inverter systems to eliminate non-detection zone," *IET Renewable Power Generation*, vol. 5, no. 2, pp. 175-183, March 2011.

[42] X. Li, "Enhanced control and protection for inverter-dominated microgrids," Ph.D. dissertation, Dept. Electron. Elect. Eng., Univ. of Strathclyde, Glasgow, United Kingdom, 2014.

[43] IEEE Standard Conformance Test Procedures for Equipment Interconnecting Distributed Resources with Electric Power Systems - Amendment 1," in *IEEE Std 1547.1a-2015 (Amendment to IEEE Std 1547.1-2005)* , vol., no., pp.1-27, 1 May 2015

[44] S. Li, T. A. Haskew, R. P. Swatloski and W. Gathings, "Optimal and direct-current vector control of direct-driven PMSG wind turbines," *IEEE Trans. Power Elec.*, vol. 27, no. 5, pp. 2325-2337, May 2012.

[45] W. Qiao, X. Yang and X. Gong, "Wind speed and rotor position sensorless control for direct-drive PMSG wind turbines," *IEEE Tran. Ind. Appl.*, vol. 48, no. 1, pp. 3-11, Jan.-Feb. 2012.

[46] S. Kouro, J. I. Leon, D. Vinnikov and L. G. Franquelo, "Grid-connected photovoltaic systems: an overview of recent research and emerging PV converter technology," *IEEE Industrial Electronics Magazine*, vol. 9, no. 1, pp. 47-61, Mar. 2015.

[47] Suleiman M. Sharkh, Mohammad A. Abu-Sara, Georgios I. Orfanoudakis, and Babar Hussain, Power electronoic converters for microgrids. Hoboken, NJ: Wiley, 2014.

[48] Aris Gkountaras, "Modeling Techniques and Control Strategies for Inverter-dominated Microgrids," Universitätsverlag der TU Berlin. 2017.

[49] T. K. Abdel-Galil, A. E. B. Abu-Elanien, E. F. El-Saadany, A. Girgis, Y. A. -R. I. Mohamed, M. M. A. Salama, H. H. M. Zeineldin, "Protection Coordination Planning with Distributed Generation," NRCAN, Varennes, QC., Technical Report CETC 2007-149/2007-09-14, Jun. 2007.

[50] J. Roberts, and A. Guzman, "Directional element design and evaluation," SEL, Pullman, WA, USA, 2006.

[51] A. Hooshyar and R. Iravani, "A new directional element for microgrid protection," *IEEE Trans. Smart Grid*, Jul. 2017.

[52] J. Horak, "Directional overcurrent relaying (67) concepts," *59th Annual Conference for Protective Relay Engineers*, College Station, TX, 2006.

[53] D. Jones and J. J. Kumm, "Future Distribution Feeder Protection Using Directional Overcurrent Elements," *IEEE Trans. Ind. Appl.*, vol. 50, no. 2, pp. 1385-1390, March-April 2014.

[54] S. H. Horowitz, and A. G Phadke, Protective Relaying Theory and Applications. New York, NY: Marcel Dekker, 2004.

[55] F. Calero, "Rebirth of negative-sequence quantities in protective relaying with microprocessor-based relays," *57th Annual Conference for Protective Relay Engineers*, College Station, TX, 2004, pp. 190-219.

[56] B. Chen, A. Shrestha, F. A. Ituzaro and N. Fischer, "Addressing protection challenges associated with Type 3 and Type 4 wind turbine generators," *68th Annual Conference for Protective Relay Engineers*, College Station, TX, 2015.

[57] J. Jia, G. Yang and A. H. Nielsen, "A review on grid-connected converter control for short-circuit power provision under grid unbalanced faults," *IEEE Trans. Power Del.*, vol. 33, no. 2, pp. 649-661, April 2018.

[58] A. Camacho, M. Castilla, J. Miret, A. Borrell and L. G. de Vicuña, "Active and reactive power strategies with peak current limitation for distributed generation inverters during unbalanced grid faults," *IEEE Trans. on Ind. Electron.*, vol. 62, no. 3, pp. 1515-1525, March 2015.

[59] T. Neumann, T. Wijnhoven, G. Deconinck, I. Erlich, "Enhanced dynamic voltage control of type 4 wind turbines during unbalanced grid faults," *IEEE Trans. Ener. Conv.*, vol. 30, no. 4, pp. 1650-1659, Dec. 2015.

[60] T. Wijnhoven, G. Deconinck, T. Neumann, I. Erlich, "Control aspects of the dynamic negative-sequence current injection of type 4 wind turbines," *IEEE PES General Meeting*, National Harbor, MD, 2014, pp. 1-5.

[61] M. S. El Moursi, W. Xiao and J. L. Kirtley, "Fault ride through capability for grid interfacing large scale PV power plants," *IET Generation, Transmission & Distribution*, vol. 7, no. 9, pp. 1027-1036, Sept. 2013.

[62] A. F. Elneweihi, E. O. Schweitzer and M. W. Feltis, "Negative-sequence overcurrent element application and coordination in distribution protection," *IEEE Trans. Power Del.*, vol. 8, no. 3, pp. 915-924, July 1993.

[63] S. Lotfi-fard, J. Faiz and R. Iravani, "Improved overcurrent protection using symmetrical components," *IEEE Trans. Power Del.,* vol. 22, no. 2, pp. 843-850, Apr. 2007.

[64] "Distribution system feeder overcurrent protection," Technical Report GET-6450, GE Power Management, Markham, Ontario, Canada, 1979.

[65] H. Lahiji, J. Mohammadi, F. Badrkhani Ajaei, R. Boudreau, "Damping power oscillation in the inverter-dominated microgrid," *18th annual IEEE Canada Electrical Power and Energy Conference (EPEC 2018)*, Toronto, ON, Canada.

[66] E. Abbasi et al., "Typical Canadian medium voltage benchmark network model for integration of distributed energy resources," *CIGRE-782*, Vancouver, BC, Canada, Oct. 2016.

[67] "Medium voltage expulsion fuses," BA/DBA fuse units, datasheet, Eaton, Aug. 2011.

Curriculum Vitae

Name:	Houman Lahiji
Post-Secondary Education and Degrees:	Western University London, ON, Canada 2016 – 2018, MESc. in Electrical Engineering University of Manitoba Winnipeg, MB, Canada 2011 – 2016, BSc. in Electrical Engineering
Related Work Experience:	• Research and Teaching Assistant, Western University, 2016 – 2018 • MITACS Accelerate position at S2e Technologies Inc., Summer 2017 • Research Assistant, University of Manitoba, Summer 2016

Publications:

- H. Lahiji, F. Badrkhani Ajaei, G. Stevens, "Modeling Short Lines for Time-Domain Simulation of the DC Microgrid," 18th annual IEEE Canada Electrical Power and Energy Conference (EPEC 2018), Toronto, ON, Canada.

- H. Lahiji, J. Mohammadi, F. Badrkhani Ajaei, R. Boudreau, "Damping Power Oscillation in the Inverter Dominated Microgrid," 18th annual IEEE Canada Electrical Power and Energy Conference (EPEC 2018), Toronto, ON, Canada.